

STABLE SUPERPARAMAGNETIC FERROFLUIDS FOR THE TREATMENT OF
SECONDARY LIVER CANCER BY HYPERTHERMIA

By

JOHN PAUL BULLIVANT

A THESIS PRESENTED TO THE GRADUATE SCHOOL
OF THE UNIVERSITY OF FLORIDA IN PARTIAL FULFILLMENT
OF THE REQUIREMENTS FOR THE DEGREE OF
MASTER OF SCIENCE

UNIVERSITY OF FLORIDA

2008

© 2008 John Paul Bullivant

ACKNOWLEDGMENTS

I thank the chair of my committee, Dr. Christopher Batich, for the opportunity to study this field. Also, for his insight and support over the years. I would like to thank various other members of the Department of Materials Science and Engineering, including the other members of my committee, Dr. Anthony Brennan and Dr. Eugene Goldberg. Dr. Kevin Powers at the PERC provided valuable help in improving the suspension of the oxides. Special thanks go to Dr. Mark Davidson of Microfabritech for all his help setting up the magnetic coil and with the XANES analysis.

Special thanks go to Dr. Joanna Collingwood of Keele University in England for performing the XANES tests, help in understanding magnetism in fine particles, and all the other advice.

The help, advice, and support of many of the different current and former members of the Batich research group has been extremely valuable. Special thanks go to Dr. Patrick Leamy for his advice and patience in helping me get adjusted to graduate school and working in the lab. I thank Jennifer Wrighton for all the things that so often are overlooked. I also thank one of our undergraduate students, Alan Kim, for his help in testing the temperature response of the ferrofluids.

I would like to thank my friends for their support, especially Matt Eadens, Matt Williams and Vishal Patel. My parents and brother have been invaluable in many ways. Finally, special thanks go to my wife Joey for the support and encouragement I needed to get things finished.

TABLE OF CONTENTS

	<u>page</u>
ACKNOWLEDGMENTS	3
LIST OF TABLES	6
LIST OF FIGURES	7
LIST OF ABBREVIATIONS.....	9
ABSTRACT.....	10
CHAPTER	
1 INTRODUCTION	12
2 BACKGROUND	14
Liver Cancer	14
Current Forms of Treatment.....	15
Detection and Diagnosis.....	16
Hyperthermia	16
Biological Effects	17
Intracellular effects.....	18
Effects on the immune system	19
Effects on blood flow	19
Medical limitations.....	19
Current Methods of Application.....	20
Magnetic Ferrofluids	22
Superparamagnetism	23
Materials in use with Ferrofluids.....	25
Effects of External Alternating Magnetic Fields on Ferrofluids	25
Heating mechanisms in SPM particles.....	25
Ideal particle size range for magnetic hyperthermia	28
Proposed Research.....	29
3 FERROFLUID SYNTHESIS AND CHARACTERIZATION	31
Ferrofluid Synthesis.....	31
Sample Nomenclature	31
Methods	32
Ferrofluid Characterization.....	35
Transmission Electron Microscopy	35
Methods.....	35
Results	36
Discussion	46

X-Ray Absorption Near Edge Spectroscopy	47
Methods	47
Results	48
Discussion	53
Superconducting Quantum Interference Device (SQUID) Magnetometry	54
Methods	55
Results	55
Discussion	56
4 HEATING OF FERROFLUIDS IN A MAGNETIC COIL	57
Resonant Circuits	57
Design of the Magnetic Coil	57
Temperature Response of Ferrofluids	59
Methods	60
Results	60
Discussion	63
5 CONCLUSIONS AND FUTURE WORK	65
Conclusions	65
Future Work	66
LIST OF REFERENCES	68
BIOGRAPHICAL SKETCH	72

LIST OF TABLES

<u>Table</u>		<u>page</u>
3-1	Detailed description of variables used in naming of ferrofluid samples	32
3-2	List of chemicals needed for production of magnetite.....	33
3-3	Linear combination fit for XANES data from sample M1-3b-9.....	48
3-4	Linear combination fit for XANES data from sample M2-4a-9.....	50
3-5	Linear combination fit for XANES data from sample M1-3a-9.....	50
3-6	Linear combination fit for XANES data from sample M1-3c-15.....	51
3-7	Linear combination fit for XANES data from sample M2-4a-9.....	52
3-8	Linear combination fit for XANES data from sample M4-4b-25.....	53

LIST OF FIGURES

<u>Figure</u>	<u>page</u>
2-1 Cartoon of injected ethiodol with suspended magnetic particles.....	21
2-2 Cartoon of a possible hysteresis curve for larger magnetic particles.....	23
2-3 Cartoon of a possible hysteresis curve for superparamagnetic particles.	24
2-4 Change in Néel and Brownian relaxation times as a function of particle size.	27
2-5 Calculated maximum susceptibility as a function of frequency and temperature	29
3-1 TEM micrograph of sample M1-3a-9.....	36
3-2 TEM micrograph of sample M1-3a-9.....	37
3-3 TEM micrograph of sample M1-3c-15.....	37
3-4 Particle size distribution for sample M1-3a-9.....	38
3-5 Particle size distribution for sample M1-3c-15.....	38
3-6 TEM micrograph of sample M2-3a-9.....	39
3-7 TEM micrograph of sample M2-3a-9.....	40
3-8 TEM micrograph of sample M4-4b-25.....	40
3-9 Particle size distribution for sample M2-3a-9.....	41
3-10 Particle size distribution for sample M4-4b-25.	41
3-11 Comparison of mean particle sizes.	42
3-12 TEM micrograph of sample M1-2a-10.....	42
3-13 TEM micrograph of sample M1-2b-15.....	43
3-14 TEM micrograph of sample M1-2b-15.....	43
3-15 TEM micrograph of sample M1-2e-30.....	44
3-16 Particle size distribution for sample M1-2a-10.....	44
3-17 Particle size distribution for sample M1-2b-15.	45
3-18 Particle size distribution for sample M1-2e-30.....	45

3-19	Comparison of mean particle sizes.	46
3-20	Linear combination fit for XANES data from sample M1-3b-9.....	49
3-21	Linear combination fit for XANES data from sample M2-4a-9.....	49
3-22	Linear combination fit for XANES data from sample M1-3a-9.....	50
3-23	Linear combination fit for XANES data from sample M1-3c-15.....	51
3-24	Linear combination fit for XANES data from sample M2-3a-9.....	52
3-25	Linear combination fit for XANES data from sample M4-4b-25.....	53
3-26	Hysteresis curves for iron oxides.....	55
4-1	Schematic diagram of the coil circuit used during the study.....	58
4-2	Image of the physical coil and connections.....	59
4-3	Heating of oil-based ferrofluids as a function of time.....	61
4-4	Heating of oil-based ferrofluids subtracting control heating.....	61
4-5	Mean heating rates for oil-based ferrofluids.....	62
4-6	Iron oxide in canola oil after settling for approximately seven days.....	62
4-7	Effect of particle settling on heating rate in sample MC1-2c-20.....	63

LIST OF ABBREVIATIONS

HCC	Hepatocellular carcinoma
TACE	Transcatheter arterial embolization
HBV	Hepatitis B virus
HCV	Hepatitis C virus
5-FU	5-Fluorouracil
LV	Leucovorin
CT	Computed tomography
MRI	Magnetic resonance imaging
US	Ultrasound
PET	Positron emission tomography
HSP	Heat shock proteins
ACMs	Antibody-conjugated magnetoliposomes
SPM	Superparamagnetic
SQUID	Superconducting quantum interference device
XRD	X-ray diffraction
XANES	X-ray absorption near edge spectroscopy
TEM	Transmission electron microscopy

Abstract of Thesis Presented to the Graduate School
of the University of Florida in Partial Fulfillment of the
Requirements for the Degree of Master of Science

STABLE SUPERPARAMAGNETIC FERROFLUIDS FOR THE TREATMENT OF
SECONDARY LIVER CANCER BY HYPERTHERMIA

By

John Paul Bullivant

May 2008

Chair: Christopher Batich

Major: Materials Science and Engineering

This study attempted to provide the ground work for the development of an alternative treatment for liver cancer using magnetically mediated hyperthermia. Iron oxide particles were synthesized and stabilized in either oil or water, forming ferrofluids. These were then characterized for size using transmission electron microscopy (TEM); the phase of iron oxide was tested using x-ray absorption near edge spectroscopy (XANES). The effective heating of the synthesized oil-based ferrofluids was tested in a custom-made magnetic coil. These tests were done against a control to examine the background heating of the system.

TEM analysis showed that some alteration of the iron chloride concentration and reaction time during iron oxide precipitation plays some role in determining the particle size. However, some of the data is inconclusive so other studies looking at particle size may be necessary. XANES analysis of the phase of iron oxide were also somewhat inconclusive. In each sample, there is some quantity of either magnetite or maghemite present, which are the expected phases. However, analysis of some samples showed the presence of other phases such as goethite and hematite. The presence of goethite indicates that the pH during iron oxide precipitation may be too high.

Heating from the magnetic coil itself appeared to be significant, as seen in the control heating. Despite this, after subtraction of this control data as background heating, at least one of the samples heated enough to be considered therapeutic.

CHAPTER 1 INTRODUCTION

Primary cancers in the liver include hepatocellular carcinoma (HCC), cholangiocarcinomas, and less commonly tumors of the hepatic vasculature such as hemangioendothelioma, hemangioblastoma, angiosarcoma, and undifferentiated primary sarcoma [1]. Of these, by far the most common form is HCC. HCC is a widespread malignancy, especially in developing countries. Recently, the trend has been toward a younger population, and increasing numbers in Asia, some areas of Europe, and Mexico [1, 2].

While primary liver cancer is getting deserved attention, another form that certainly has need of an improved treatment is secondary, or metastatic, liver cancer. Due to the nature of the liver, filtering the blood, it is a common site for metastasis to occur from other forms of primary cancer. Of special note is that with colorectal cancer, ranking as the second leading cause of death due to cancer, the main cause of death is due to liver metastasis. The chance of getting colorectal cancer at some point in one's lifetime is approximately 5%, with the incident rate approximately 50 per 100,000 [3]. By the time colorectal cancer is detected, approximately 15 to 25% of patients will already have liver metastases, and another 20% will develop metastases following treatment for the colorectal cancer [3, 4]. Over 50,000 patients a year are diagnosed with liver cancer metastasized from colorectal cancer alone [5].

Current treatments for liver cancer include surgical (resection), chemotherapy, various ablative methods, percutaneous ethanol injection and transcatheter arterial embolization (TACE). Resection is recognized as the gold standard because it offers the most reliable chance of curing the patient [3]. However, it is not always an option, especially for patients with secondary liver cancer. Chemotherapy can cure these cancers, but this technique has had less success with liver cancer as compared to other forms of cancer. This is improving as the targeting of drugs to

tumors gets better, but as of 2002, the median survival was only approximately 12 to 17 months depending on the treatment used [3]. In most cases, it is used in concert with other forms of treatment [6]. Perhaps the biggest advantage to using chemotherapy is that following chemotherapy, some patients who were previously ineligible for resection are then able to undergo resection, increasing their chances of survival.

The goal for this project was to partially develop a potential alternative treatment that could be used either alone or in combination with other treatments. The idea behind this treatment is to preferentially target the tumors with iron oxide particles that can be heated using an external magnetic field. If the heating is sufficient, apoptosis, or programmed cell death, can be induced without causing necrosis. Known protocols for the manufacture of these particles were to be modified to tailor their stability in suspension, size, and magnetic properties. They were then to be characterized to determine the size and phase of the particles. Finally, the response of the particles to an external AC magnetic field was tested with the goal of reaching temperatures high enough to induce apoptosis.

CHAPTER 2 BACKGROUND

Liver Cancer

HCC has several kinds of causes, including physiological ones like those listed above, as well as viral, dietary, and hormonal/chemical factors [2]. The viral causes are dominated by hepatitis B and hepatitis C (HBV and HCV respectively). HBV was shown to be a cause simply through population studies: where there is a high prevalence of HBV, there is a high incidence of HCC [2]. This is especially true in Asia, where many have acquired HBV in childhood. HCV was identified as a cause due to the correlation between the development of cirrhosis followed by HCC in patients having HCV from blood transfusions [2].

The dietary factors include aflatoxin B₁, which can be ingested with contaminated food, and alcohol. The evidence for aflatoxin is not as strong as with other factors, but areas where there is a high incidence of HCC correlate with those where contamination of aflatoxin is a problem, mostly in Asia and southern areas of Africa [2]. However, it can be noted that Asia especially is an area where other factors such as hepatitis play a large role. Because of this, establishing just how large a factor aflatoxin plays is difficult at best. Alcohol has shown to have a clear association with cirrhosis, which has been shown to be common in many before HCC is diagnosed [7]. In the US, where HBV is relatively uncommon, the risk of HCC has been shown to be 40% higher in those who drink heavily [2].

Various hormones and chemicals are also responsible for increased risk of HCC. Several controlled studies have shown a correlation between the long-term use of oral contraceptives and HCC. One study shows that employment in fields dealing with rubber, PVC or hydrocarbons is a potential risk for HCC [2].

Studies show that between 1980 and 1995, the incident rate for HCC almost doubled, from 1.4 per 100,000 to 2.4 per 100,000 [8]. With hepatitis C becoming a greater problem every day, some estimate that this will double once again by 2025 [9].

Current Forms of Treatment

Resection is mostly used as an option for patients with primary liver cancer, such as HCC. In this case, however, it is often complicated by cirrhosis, because the liver then has little regenerative capability. As such, the surgery must be very well planned so that little healthy liver tissue is lost, and that as little blood is lost as possible [10]. In about 15% of patients with secondary liver cancer, resection is an option and is then used with some success. Five year survival rates vary from 21 to 50% assuming the margins for resection are large enough [3]. However, these statistics drop down to 0 to 17% if there is only a small or negligible margin. This does not mean that cutting away large portions of the liver is a good choice. In many cases, a second resection is necessary, in which case it benefits the patient greatly if more of the liver were spared in the first surgery [3].

In Europe as of 2002, chemotherapy was still the first line of treatment for liver cancer. This treatment was mostly based on 5-fluorouracil (5-FU), and more recently with incorporation of leucovorin (LV), irinotecan and oxaliplatin [3]. Response rates in trials were seen to increase with the incorporation of the other drugs into the treatment (20% to 50%), and survival length increased from a median of 12 months to 17 months. However, both irinotecan and oxaliplatin both increased the incidence of complications due to toxicity, meaning that many consider 5-FU/LV to be the standard regimen [3].

In most patients, the other forms of treatment are usually palliative, meaning a reduction in symptoms but no real cure. Some of the alternative treatments include percutaneous ethanol injection, cryosurgery, radiofrequency ablation, laser interstitial thermal therapy, isolated hepatic

perfusion and focused ultrasound. The best of these can in some cases offer survival rates close to that of resection. However, there are often large complications that make the risk of using these techniques significant.

Detection and Diagnosis

Detection and diagnosis of secondary liver cancer continues to have much room for improvement. There have been vast strides made in recent years, especially due to the increase in resolution in various imaging methods allowing smaller sectioning. The majority of scanning is done with computed tomography (CT), magnetic resonance imaging (MRI), ultrasound (US), positron emission tomography (PET). There is no clear consensus as to the best method to use.

US is popular due to the low invasiveness and cost, but it is highly operator dependent and in some patients, parts of the liver may not be clearly visualized [11]. As such, it plays a useful role in the initial search for symptomatic patients but is not as useful as a screening technique. Helical scan CT with modern iodinated contrast agents is typically the method of choice for determination of the stage of the tumor. These contrast agents include commercial products such as Visipaque and Omnipaque. If the patient has contraindications to iodinated contrast agents or severe hepatic steatosis, gadolinium-enhanced MRI is usually used [11]. MRI is also useful in distinguishing between metastases and small cysts. PET with 18-FDG as a contrast agent is another alternative, although recent research shows that the sensitivity is not as high as first thought [11].

Hyperthermia

Hyperthermia, literally a rise in temperature, has been recorded as a treatment for various ailments since the times of Egypt, Greece and Rome, as early as 2000 BC [12]. Hippocrates himself noted that “illness not cured by heat is incurable.” This enthusiasm for using heat lessened during the 16th century when Ambrose Pare demonstrated that cauterization caused

“unacceptable consequences” [13]. However, as doctors and scientists began to understand more about the human body and its response to heat, hyperthermia saw more interest. Julius Wagner-Jauregg noted in his Nobel work that patients with malaria, and the fever associated with it, had a lower incidence of syphilis. Many advances have been made since this time, both in the understanding of the body’s response to the application of heat, and in how to effectively apply it.

Biological Effects

The exact temperature range in which hyperthermia is therapeutic is still somewhat debated. The effects of temperature with time vary somewhat by cell line, and the local conditions, such as pH, blood flow, and thermal tolerance [14, 15]. However, it is generally understood that temperatures between 41 to 42°C, when held for at least 30 minutes, will be lethal to tumor cells while not damaging healthy cells [16]. In 2002, the World Health Organization met to discuss ‘adverse temperature levels in the human body.’ While this meeting was primarily to establish guidelines for RF exposure in the range from 10 to 300 GHz, it did much in raising awareness of the relationships between temperature levels, time exposure, and tissue damage [17]. When looking at Chinese hamster ovary cells, Sapareto et al. found that below 43°C, a four-fold increase in time was needed per degree below 43°C. Above 43°C, however, they noticed a two-fold decrease in time needed per degree to achieve the same levels of damage [18]. Similarly, cell survival decreased dramatically above 43°C. At higher temperatures, necrosis becomes more common, though the temperature at which this is likely dependent on many factors.

The exact mechanism whereby cell damage takes place is not fully understood, though several contributing factors have been suggested. There is evidence that more oxidizing agents are generated, including superoxide [19]. Oxidation was seen in lipids, proteins, and DNA. At

this point, studies suggest that protein denaturation is the primary cause of cell death [17, 20, 21]. While the activation energies for metabolic reactions are lower (3 to 20 vs. 100 to 200 kcal/mol), there is little evidence to suggest even long-term exposure causes enough of an unbalanced metabolism to cause permanent damage [17]. Due to denaturation, proteins are then more likely to aggregate, which unless reversible can cause cell death [20].

Intracellular effects

There is some debate as to whether the cell is most sensitive to damage during the S phase or M phase, but it is clear that the cell is vulnerable to lower heat levels during these phases than during the G1 phase [15, 21]. During the S phase, DNA fragments are likely to join incorrectly, causing the cell to undergo apoptosis during mitosis [15]. M phase cells have shown damage to the mitotic apparatus, meaning inefficient mitosis and then polyploidy [21]. During the G1 phase, studies show that the cell is somewhat more resistant to the effects of heat, up to approximately 46°C [22]. Above this temperature, disruption of the cell membrane appears to be the primary cause of cell death in this phase, although the mechanism is somewhat unclear [15].

One area in which there is no debate is that as a result of hyperthermia, synthesis of heat shock proteins (HSPs) occurs. This class of proteins plays many roles in normal cell function, including protein assembly (as molecular chaperones), signal transduction, and cell growth and differentiation [19]. In the case of hyperthermia, 70 kDa HSPs (HSP70s), the primary chaperones, appear to play the most critical role [19, 20]. By binding proteins, HSP70s help prevent aggregation, meaning that it can be reversible. As a result, cells in which HSPs are upregulated are more resistant to future hyperthermia treatments, by as much as 4 to 10 times [15]. This thermotolerance can last anywhere from a few hours to a few weeks [15]. As such, high initial heating rates are desirable to minimize the presence of HSPs before a therapeutic

temperature is reached. However, exacting control of the applied temperature is necessary in order to level off the temperature at the desired values and avoid causing necrosis.

Effects on the immune system

With moderate (at or below 42°C) hyperthermia, there is evidence that the immune system is stimulated [15, 21]. Burd et al. noticed an accumulation of host lymphocytes and NK cells, while others have noticed increased interferon levels [23]. However, with increased temperature, NK lymphocyte count was lower [24].

Effects on blood flow

One of the leading factors in complicating models of hyperthermia is the differing blood supplies to tumors. The biggest changes in comparison to the normal vascular system are seen near the center of the tumor, which is characterized by abnormal branching and sluggish blood flow [15]. The typical response of healthy tissue to hyperthermia is an increase in blood flow, dissipating excess heat and reducing damage. In contrast, studies show that in tumors, with hyperthermia above 42°C, blood flow either decreases significantly or ceases in places, further reducing the oxygen content and pH [15]. However, with hyperthermia below 42°C, some studies have shown an increase in blood flow, decreasing the effectiveness of the treatment [21].

Medical limitations

Several studies have been done in the past that indicated potential damage to human tissue with exposure to alternating magnetic fields. Of these, Atkinson *et al.*'s work has become accepted as describing the safe limits of magnetic fields that can be applied to humans [25]. In their research, they found that fields up to 35.8 A/m at 13.56 MHz could be tolerated for extended periods of time. Since the heating of tissue is proportional to $H \cdot f$, they concluded that exposure to magnetic fields would be safe as long as the product $H \cdot f$ does not exceed 4.85×10^8

A/(m s), or 6.09×10^6 Oersted. Admittedly this research was performed at frequencies far above what is considered to be ideal for use in hyperthermia, but to date it is considered the safe limit.

Current Methods of Application

There are two broad categories in application of hyperthermia, in which the whole body or specific regions are treated. Current research in the field of hyperthermia directed more in targeted treatments, though there is still a great deal of room for improvement. As with other forms of cancer treatment, many of the targeted treatments are designed for a specific form of cancer. In general, the more targeted treatments allow for less side effects, and also more frequent treatment. Some of the untargeted treatments include whole body, RF capacitance, microwave and isolated hepatic perfusion. Targeted hyperthermia treatments include RF probe, interstitial laser, direct injection, magnetically mediated and focused ultrasound.

As the goal of this research is to improve the work in magnetically mediated hyperthermia, previous work done in this field is of special interest. This technique is based on the idea that magnetic materials can be heated by using an oscillating magnetic field, inducing hyperthermia. The mechanisms by which these materials heat will be described later. Various groups have approached the technique in different manners, mostly relating to the way in which they attempt to target the tumor but also in particle size, shape, and phase of iron oxide.

Jones and his students focused primarily on arterial embolization hyperthermia, in which the blood supply is used as the targeting mechanism [26]. This is especially of use with liver cancer due to the nature of the circulatory system. Particles for these studies were generally ~ 100 nm maghemite in ~ 30 μm polymer microspheres. *In vivo* tests on rabbits showed that there was a 50 to 94% decrease in tumor volume. This technique is primarily focused on larger tumors that have an established blood supply.

Jones also examined suspensions of maghemite in ethiodol. Ethiodol is an alternative contrast agent for CT scans that is still in use. It is a mix of iodinated ethyl esters of fatty acids from poppyseed oil. The exact structure is unknown, as some chains have one double bond before reacting with iodine and some two. As a result, some of the molecules have one iodine atom attached, and some have two. Because of the high atomic number of iodine, it acts as a good contrast agent in CT scans. In the mid-1980s, several groups examined the use of ethiodol as a method of identifying HCC [27, 28]. After injection into the hepatic artery, ethiodol embolizes the capillary beds. Approximately 3 to 7 days after injection, tumors were noticeable [29]. A cartoon of this injection is shown in Figure 2-1.

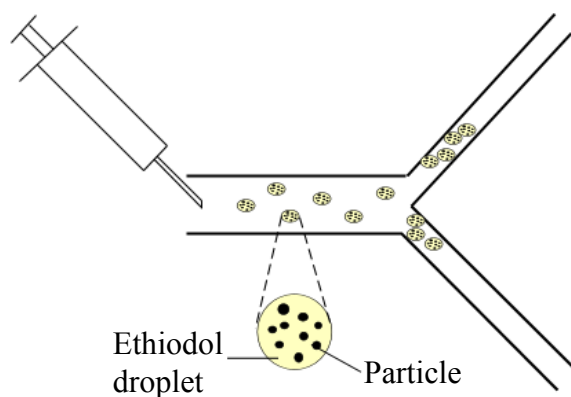


Figure 2-1. Cartoon of injected ethiodol with suspended magnetic particles.

The tumors become more obvious with time, as ethiodol is cleared by the healthy parenchyma, hepatic lymphatics and Kupffer cells within about four weeks, whereas in cancer cells, the ethiodol can be seen for up to a year [30]. The smallest tumors that could be seen at that point ranged from about 2.5 to 3.5 mm [30]. This research sought to use ethiodol as a delivery agent for the maghemite particles.

In vivo studies on pigs by this group examined the clearance of magnetic particles through the liver, looking at a suspension of 150 nm maghemite particles in ethiodol [31]. A total of 300

mg of maghemite was placed in 6 mL ethiodol. Observations showed that little of the oxide was processed by the liver, healthy or not. In healthy regions of the liver, the particles were heavily phagocitized but still present. For their study, concentrations in other areas of the body were as follows: pancreas 0.04 mg/g; spleen 0.53 mg/g; duodenum 0.05 mg/g; stomach 0.05 mg/g; kidney 0.07 mg/g; lung 0.08 mg/g. Since magnetic hyperthermia relies on there being a large difference in concentration of oxide between healthy liver cells, this is of great concern for this technique. However, considering the size of these particles, it is likely worth re-examination with smaller particles.

A Japanese group led by Kobayashi has been working on cationic liposomes, some conjugated with antibodies (ACMs) to allow the targeting of tumors [32, 33]. Non-crosslinked liposomes were injected directly into a mouse melanoma with complete regression seen in up to 90% of the mouse population [34]. For deeper tumors, they suggested that ACMs would be a more effective treatment.

Magnetic Ferrofluids

While much of this project is related to magnetism, this paper will focus on magnetism as it relates to small particle ferrofluids rather than the field of magnetism as a whole, which has already been reviewed in many excellent texts such as those by Jiles and Morrish [35, 36]. For the purposes of this study, magnetic ferrofluids are some form of iron oxide in a stable suspension in either oil or water. These particles are often magnetite (Fe_3O_4) or maghemite ($\gamma\text{Fe}_2\text{O}_3$), and are usually stabilized by attaching some form of surfactant to the surface. For these materials, the magnetic properties of the particles vary greatly from approximately 5 to 100 nm in diameter and these in turn dictate to some extent which materials are used and the size of the particles.

Superparamagnetism

At the larger end of this size range, magnetic particles typically have more than one magnetic domain and act as if they were a bulk magnetic material. As you decrease the particle size, there becomes a point at which the particle only has one magnetic domain. Further decreasing the particle size, there becomes a point at which the particle is no longer considered to be magnetically blocked. In this case, the magnetic domain rotates at random due to thermal energy. Below this size, the particle is considered to be superparamagnetic (SPM). The particle size that this transition takes place is dependent on the material in question and the external temperature. For magnetite, the particles become single domain at approximately 50 nm, and SPM at approximately 25 nm [37].

SPM particles exhibit no remnant magnetization in the absence of an external magnetic field. For AC magnetic fields, this is usually shown in terms of hysteresis loops, as shown in Figures 2-2 and 2-3. In both plots, the external magnetic field (H) at the start is zero, as is the magnetization (M). As the magnetic field increases in strength, the magnetization increases to

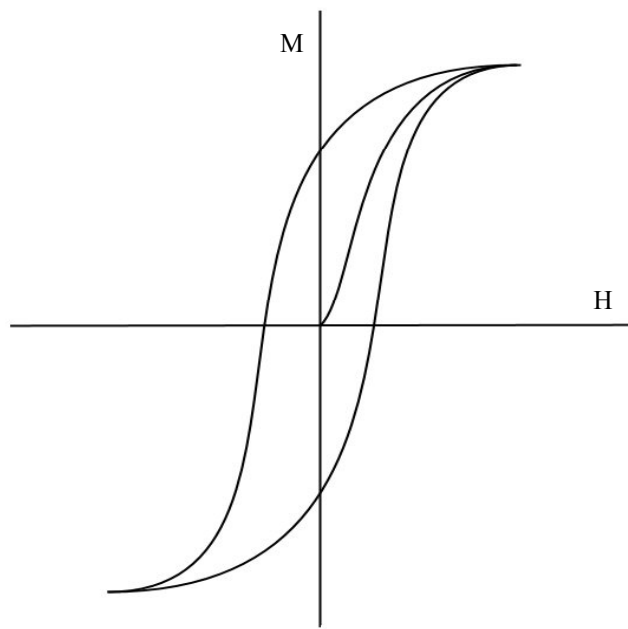


Figure 2-2. Cartoon of a possible hysteresis curve for larger magnetic particles.

follow until it eventually reaches the saturation magnetization. In bulk magnetic materials, when the magnetic field is decreased, the magnetization decreases but does not return to zero when there is no field applied. When the magnetic field is reversed, the magnetization continues to increase in the opposite direction, again until it reaches the saturation magnetization. The area within the curve is due to the energy required to change the direction of adjacent magnetic domains, which often are opposing in nature. For SPM materials, on the other hand, the magnetization returns to zero when the external magnetic field is removed.

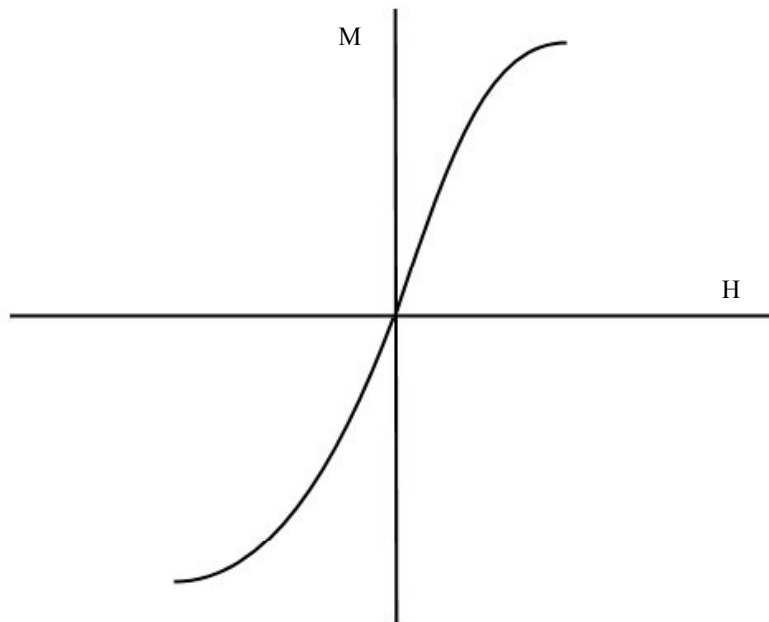


Figure 2-3. Cartoon of a possible hysteresis curve for superparamagnetic particles.

For use with hyperthermia, these magnetic properties are desirable for several reasons. Due to the lack of a remnant magnetic polarization, there is less likelihood of the particles agglomerating. This is beneficial in that there is less chance for embolization, the particles are more likely to remain in suspension, and the ferrofluid is easier to inject. Also, the heating is more efficient at smaller particle sizes when limited to small field strengths. The processes by which these particles heat will be discussed later.

Materials in use with Ferrofluids

The most common materials in use for ferrofluids are magnetite, which is Fe_3O_4 , and its oxidation product maghemite, which is $\gamma\text{-Fe}_2\text{O}_3$. Magnetite is also known as lodestone, and is a naturally magnetic material. It has an inverse spinel structure, with Fe^{2+} ions occupying only octahedral sites, and Fe^{3+} ions split evenly between tetrahedral and octahedral sites. The Fe^{3+} ions in the octahedral and tetrahedral sites have opposite spins, meaning a zero net magnetic moment. The net magnetic moment can therefore be determined by examining the net magnetic moment of the Fe^{2+} ions [38]. Due to this structure, magnetite is ferrimagnetic.

Maghemite has similar magnetic properties but the structure differs slightly. Instead of an inverse spinel structure, it has a spinel structure with cation vacancies. It is also considered to be a ferrimagnetic material [39].

Effects of External Alternating Magnetic Fields on Ferrofluids

For use with hyperthermia, the goal with ferrofluids is to release as much energy in the form of heat as possible. In larger particles, the maximum amount of heat given off is higher than in SPM particles due to the higher saturation magnetizations. For these particles, the heat given off per unit volume is proportional to the frequency multiplied by the area within the hysteresis curve. However, within the safe limits on field strength, these magnetic materials will never reach the saturation magnetization. For SPM materials, however, the mechanism for heating is different and results in higher heating rates at usable field strengths [40].

Heating mechanisms in SPM particles

Several authors have gone into detail on the mechanisms of heating for magnetic materials in alternating magnetic fields. Perhaps the most cited in the hyperthermia literature is Rosenweig, who used the Debye model to look at the heat dissipation due to rotational relaxation [41]. Heating due to eddy currents is assumed negligible in this model. The magnetization of

the particles lags behind the external field. Assuming little interaction between particles, the magnetization of the particles in an AC magnetic field can be described by its complex susceptibility:

$$\chi = \chi' - i\chi'' \quad (2-1)$$

Upon further analysis in substitution into equations for internal energy, only the out-of-phase component survives yielding the following equation:

$$P = f\Delta U = \mu_0\pi\chi'' fH_0^2 \quad (2-2)$$

where P is the power, f is frequency, U is internal energy, μ_0 is the permeability of free space, H_0 is the equilibrium field strength. Of note in this is that the power is proportional to the square of the field strength. As the product of the field strength and frequency is limited for human use, this is a key factor in determining the range of field strengths and frequencies that are commonly used. Further, the out-of-phase susceptibility can be defined as

$$\chi'' = \frac{\omega\tau}{1 + (\omega\tau)^2} \chi_0 \quad (2-3)$$

with τ being the relaxation time and χ_0 being the equilibrium susceptibility. Substituting this into Equation 2-2 gives

$$P = \pi\mu_0\chi_0 H_0^2 f \frac{2\pi f\tau}{1 + (2\pi f\tau)^2} \quad (2-4)$$

which maintains that the field strength is far more important than frequency in optimizing heating rate.

The relaxation time is defined by two mechanisms, known as Brownian relaxation and Néel relaxation. Brownian rotation occurs when the magnetic moment is locked to the physical particle. When the magnetic moment rotates to align with the magnetic field, the particle rotates with it. Néel rotation, on the other hand, is rotation of the magnetic moment alone, resulting in

no rotation of the particle itself. As such, this form of relaxation contributes little heating to the system and must be minimized [41]. The total relaxation time can be defined as

$$\frac{1}{\tau} = \frac{1}{\tau_B} + \frac{1}{\tau_N} \quad (2-5)$$

where τ_B is the Brownian relaxation time and τ_N is the Néel relaxation time. Examining this shows that the shorter of the two relaxation times will tend to dominate the expression. The relationship between these two types of relaxation and particle size for magnetite are shown in Figure 2-4, in which the Néel relaxation time increases dramatically as particle size increases.

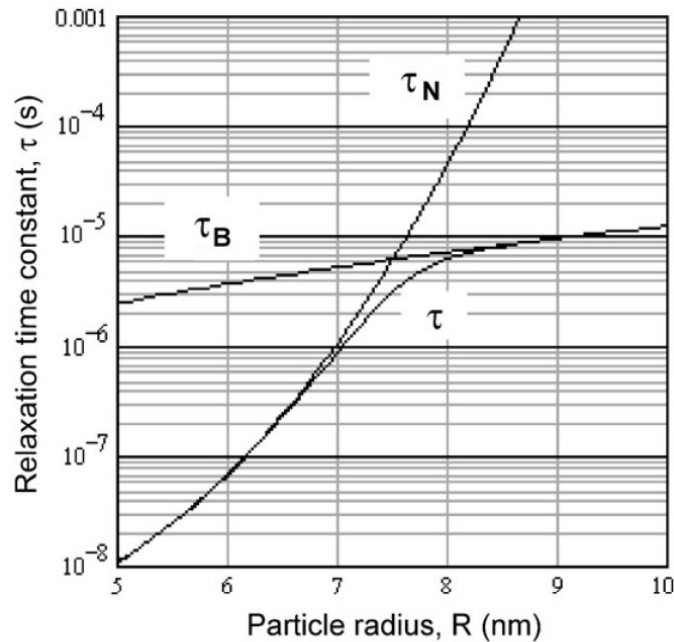


Figure 2-4. Change in Néel and Brownian relaxation times as a function of particle size for magnetite. Reproduced from Figure 2 in Rosenweig [41].

Examining Equation 2-5, this means that the smaller increase in the Brownian relaxation time means the contribution from Brownian rotation will begin to dominate the expression at approximately 7.5 nm in diameter for magnetite.

The Brownian relaxation time is given by

$$\tau_B = \frac{3\eta V_H}{kT} \quad (2-6)$$

where η is the viscosity, V_H is the hydrodynamic volume, k is Boltzmann's constant and T is the temperature in Kelvin. While the particle size itself is different from the hydrodynamic volume, it shows the importance of controlling particle size and limiting the size of a surfactant. On the other hand, the use of no surfactant would lead to agglomeration, meaning far larger hydrodynamic volumes and far less heating overall.

Ideal particle size range for magnetic hyperthermia

The ideal particle size range for use with hyperthermia is defined by several factors. As shown in the previous discussion, to prevent Néel relaxation from being the dominant mechanism, the particle size should be at least eight nm in diameter in the case of magnetite. However, the particle size cannot be allowed to grow too large or the hydrodynamic volume will increase significantly. The optimum size will depend on the system in use, especially the frequency being used. Figure 2-5 shows the calculated maximum susceptibility for two sizes of magnetite particles. In this calculation, χ'' was found to be maximized when $2\pi f\tau = 1$ [42]. Essentially, within this range from 7 to 11 nm, the larger particles are better suited for use at about 300 to 400 kHz whereas the smaller particles are better suited for use at about 70 MHz.

While it would be good to minimize the frequency in order to maximize the field strength, this means larger particles would be necessary. As shown in Equation 2-6, τ_B is proportional to the hydrodynamic volume. Since the hydrodynamic volume is proportional to the radius cubed, even a small change will result in a large increase in τ_B . Eventually the $(\omega\tau)^2$ term in the denominator of Equation 2-3 begins to dominate and as a result, χ'' decreases. This balance between hydrodynamic volume and frequency means that there is a range of sizes which generate good heating. This range is from approximately 8 to 20 nm in diameter, with corresponding frequencies in a range from approximately 50 kHz to 1 MHz.

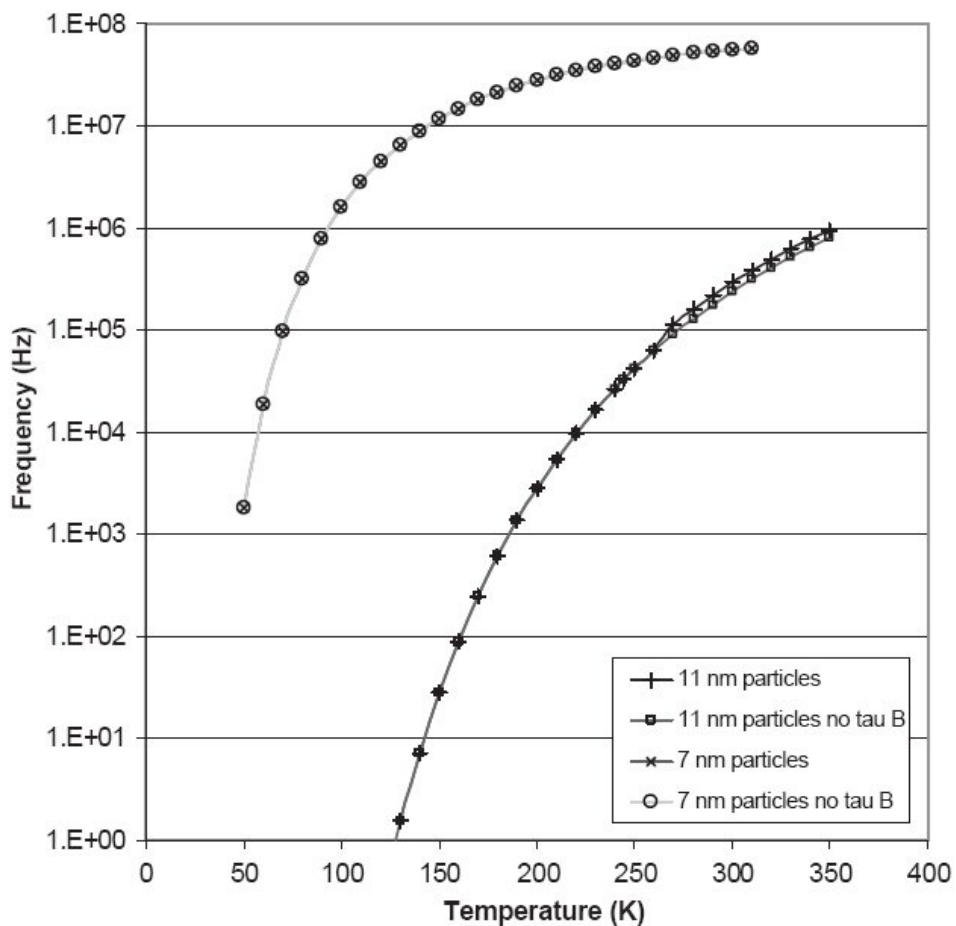


Figure 2-5. Calculated maximum susceptibility as a function of frequency and temperature for two sizes of magnetite particles. Measurements are for the particle diameters. Reproduced from Gonzales and Krishnan, Figure 6 [42].

Proposed Research

As compared to other forms of cancer, including primary liver cancer, the death rate is higher and there are more problems associated with the treatment of secondary liver cancer. As such, improving the treatment of secondary liver cancer will be the main goal of this study, though in all likelihood it will apply to primary liver cancer too for patients who are not candidates for resection.

While magnetically mediated hyperthermia has been studied both *in vitro* and *in vivo* before, in many cases there has been little attempt to optimize the particles made for the

ferrofluid. The vast majority of researchers follow protocols for the precipitation of magnetite that have been established for different systems (ex. different frequencies and field strengths). As such, when applied to the system in use for research, the particles are commonly not optimized for that system. At best this has led to somewhat inefficient heating and at worst has sometimes led to the use of magnetic fields that have been shown unsafe for human use in order to achieve the desired results [26, 32].

This research attempts to characterize and optimize magnetic particles for use with magnetic hyperthermia. This optimization was primarily focused on particle size and stability in both water and oil. The oil-based ferrofluids were tested to measure their thermal response to AC magnetic fields with the intention of achieving therapeutic heating. Restrictions were placed on the magnetic field strength such that it was well within the safe limits.

CHAPTER 3 FERROFLUID SYNTHESIS AND CHARACTERIZATION

Ferrofluid Synthesis

Ferrofluid synthesis has seen a fair amount of interest in the literature in recent years. While there have been several types of oxides various groups have attempted to synthesize, the majority intending to use the ferrofluid attempt to make magnetite or maghemite due to the high saturation magnetizations. Several studies have identified reagents, their concentrations in solution, and both reaction temperature and time as key variables in determining the size, size distribution and shape of the particles formed.

Within this research group, the focus has been on magnetite, although oxidation often results in at least some of the product being maghemite. Although characterization of the oxides produced by Dr. Patrick Leamy was somewhat inconclusive as to the phase of iron oxide produced, SQUID magnetometry showed conclusively that the particles were SPM [43]. Some of these results will be shown here as the primary changes to this method resulted in slightly smaller particles than were produced for that study.

Sample Nomenclature

Sample nomenclature differentiates between the media the iron oxide is suspended in, the concentration of iron chloride solutions, the procedure used, the individual sample and the reaction time. The scheme for the letters and numbers that differentiate these synthesis variables is, in general either MX-YA-ZZ for aqueous systems, or MCX-YA-ZZ for those in canola oil. For this scheme, X represents the concentration of iron chlorides used, Y represents the procedure used, A represents the individual sample letter for that procedure, and ZZ represents the reaction time, in minutes. In cases where all variables are identical except that one is reported as M and the other MC, the particles are identical but the M- particles have a double

layer of oleic acid coating as compared to a single layer for MC-. A more detailed comparison of the specific meaning of those variables is given in Table 3-1.

Table 3-1. Detailed description of variables used in naming of ferrofluid samples

Variable	Values	Description
X	1	4.35 g FeCl ₃ :1.60 g FeCl ₂
	2	2.52 g FeCl ₃ :1.05 g FeCl ₂
	4	8.70 g FeCl ₃ :3.20 g FeCl ₂
Y	2	Describes the addition of all oleic acid before reaction takes place.
	3	Only 0.1 mL oleic acid is added initially with acetone. More is added at regular intervals that were altered to attempt to control particle size. For MX-3a and -3b, 0.2 mL of oleic acid was added after 5 min. and the reaction stopped at 9 min. For M1-3c-15, 0.2 mL was added at 7.5 min and 12.5 min.
	4	Similar to Y=3 except oxide is dispersed in ethanol/water instead of water only after washing oxide.

Methods

The methods used for this study were adapted from that in Leamy's PhD dissertation and Chen *et al.*'s analysis of when and what quantities of concentrations of oleic acid to add to achieve a stable oil-based suspension [43, 44]. Leamy's method was modified first in when the addition of oleic acid is made. Further, instead of adjusting the molar ratios of Fe²⁺ and Fe³⁺ to control oxidation, the precipitation was done under argon. This allowed the molar ratios to be adjusted to 2:1 for Fe³⁺:Fe²⁺, which is consistent with the molar ratio seen in magnetite. For modification to allow suspension in water, Maity and Agrawal's method was followed almost exclusively [45]. Magnetite cannot simply be precipitated in aqueous solution and be expected to form a stable suspension as the zeta potential at neutral pH is only slightly negative. This repelling force is not strong enough to overcome Van der Waals forces, resulting in significant agglomeration. Both the aqueous and oil-based ferrofluid procedures are identical in the initial steps. A list of the chemical reagents used is shown in Table 3-2.

Table 3-2. List of chemicals needed for production of magnetite

Chemical name	Source	Grade
Ferrous chloride tetrahydrate	Aldrich	99%
Ferric chloride hexahydrate	Aldrich	98%
37% HCl (aq.)	Acros	
29% Ammonium hydroxide	Aldrich	
Oleic acid	Aldrich	Tech. grade, 90%
Methanol	Fisher	Lab. grade
Ethanol	Fisher	
Acetone	Fisher	
Canola oil	Wesson Oil	

For the M1-2 and MC1-2 series of particles, 130 mL of DI water in a 250 mL beaker was heated to 80°C. As oleic acid must be refrigerated, during which it solidifies, it was defrosted while the water was heating. Next 4.35 g of ferric chloride hexahydrate and 1.60 g of ferrous chloride tetrahydrate were added to 20 mL of a 5% HCl solution. Then, 0.4 mL of oleic acid was added to 5 mL acetone. After the DI water had reached the desired temperature, argon was slowly bubbled in to help prevent oxidation during the formation of the iron oxide. A mechanical stirrer with a four-bladed stainless steel attachment was used to stir the water at 150 RPM. The acidic solution of iron chlorides was then added, followed shortly by slowly adding the acetone. This solution was allowed to stir for two minutes before increasing the stir rate to 350 RPM. At this point, 8.5 mL of 29% NH₄OH was added, immediately changing the color of the solution to black as the iron oxide precipitated. The solution was allowed to stir for a specific amount of time, varied according to the desired particle size.

After the reaction was complete, the beaker was removed from heat and stirring, allowing the solution to cool briefly until it could be held. Note that this extra time should be kept to a minimum as the reaction will continue, albeit at a slightly slower rate. The oxide was collected at the bottom of the beaker with a magnet and the supernatant decanted. To wash the oxide, it was then redispersed in 10 mL methanol, followed by adding 10 mL acetone to flocculate. The

oxide was then collected again with the magnet, and the supernatant decanted. This was repeated one more time to remove any excess reactants and any oleic acid not attached to the surface of the oxide. At this point, the total weight of oxide plus oleic acid and associated methanol was approximately 2 g. After this point, the remainder of the process for resuspending the oxide in water or oil differs.

Since there is a monolayer of oleic acid on the surface, resuspension in a good organic solvent for oleic acid could be achieved by simply adding the oxide directly to that solvent. This is ideal for long-term storage of the oxide as it often results in the most stable suspensions. For this procedure, canola oil was used as a substitute for ethiodol due to its similar chemical structure. Because the oxide does not readily disperse directly into this oil, a few intermediary steps were added. First, 0.4 mL of oleic acid was added to 30 mL of ethanol in a 250 mL beaker. Although there should be a monolayer on the surface of the oxide at this point, it is a somewhat reversible attachment, so more is added to make sure that a monolayer is maintained. The oxide was then added to the ethanol with slight agitation to redisperse the particles. This ferrofluid was then stirred using the mechanical stirrer at 150 RPM. While stirring, 0.25 mL oleic acid was added to 20 mL canola oil. After stirring for five minutes, the canola oil was added slowly to the ferrofluid. After another five minutes the stir rate was reduced to 100 RPM and the ferrofluid left overnight to allow the ethanol to evaporate.

Resuspension of the coated oxide in water is at this point more complicated as the particles are now quite hydrophobic. First, a basic solution of oleic acid was prepared by adding 3 mL NH_4OH and 4 mL oleic acid to 40 mL DI water. Note that this will take some time to dissolve so it is often useful to perform this step while the oxide is reacting. 40 mL ethanol was added to 40 mL DI water in a 250 mL beaker. The washed oxide was then added to this solution and set

up to stir at 250 RPM and 60°C under argon. The aqueous solution of oleic acid was then pipetted slowly into the ferrofluid. After this solution was added, heating was continued for 15 minutes. The solution was then removed from heat, while stirring at 100 RPM overnight under argon.

Ferrofluid Characterization

Characterization for ferrofluids is needed in several areas: determining the actual material produced, its magnetic properties, and the quality of the suspension. Not knowing these properties gives an incomplete understanding of the product and also the validity of the data gathered. While the tests performed during this study are not all-encompassing, they at minimum allow a good understanding in each of these areas.

Transmission Electron Microscopy

For these ferrofluids, transmission electron microscopy (TEM) allowed visual confirmation of the size of the iron oxide particles, their shape, and to some extent an ability to estimate the coverage of the oleic acid coating. In comparison to light-scattering methods, there is no complication due to agglomeration of particles. That analysis is extremely useful in examining the hydrodynamic volume of particles, but for analysis of the magnetic response it was more useful at this stage to examine the size of the iron oxide cores.

Methods

Aqueous ferrofluid samples were diluted from 20 μL to 2 mL. 20 μL of the diluted sample was then pipetted onto a carbon film on a copper grid sitting on filter paper. Excess sample was absorbed by the paper, and that remaining on the grid was allowed to evaporate overnight, covered by a petri dish to help prevent contamination.

The microscope used was a JEOL JEM 2010F, at an accelerating voltage of 200 kV. Particle sizes were measured using ImageJ by drawing through the diameter for each

recognizable particle. This data was then exported to Microsoft Excel and Graphpad Prism for analysis. In each case, approximately 200 particles were measured for analysis.

Results

The first modification to Leamy's method of particle precipitation was to add a small quantity of oleic acid in acetone. An initial attempt to control the size of the magnetic particles was made by varying the timing of adding the remaining oleic acid. For sample M1-3a-9, 0.2 mL of oleic acid was added five minutes into the reaction. For sample M1-3c-15, 0.2 mL of oleic acid was added at 7.5 and 12.5 minutes. Micrographs for these samples can be seen in Figures 3-1 to 3-3.

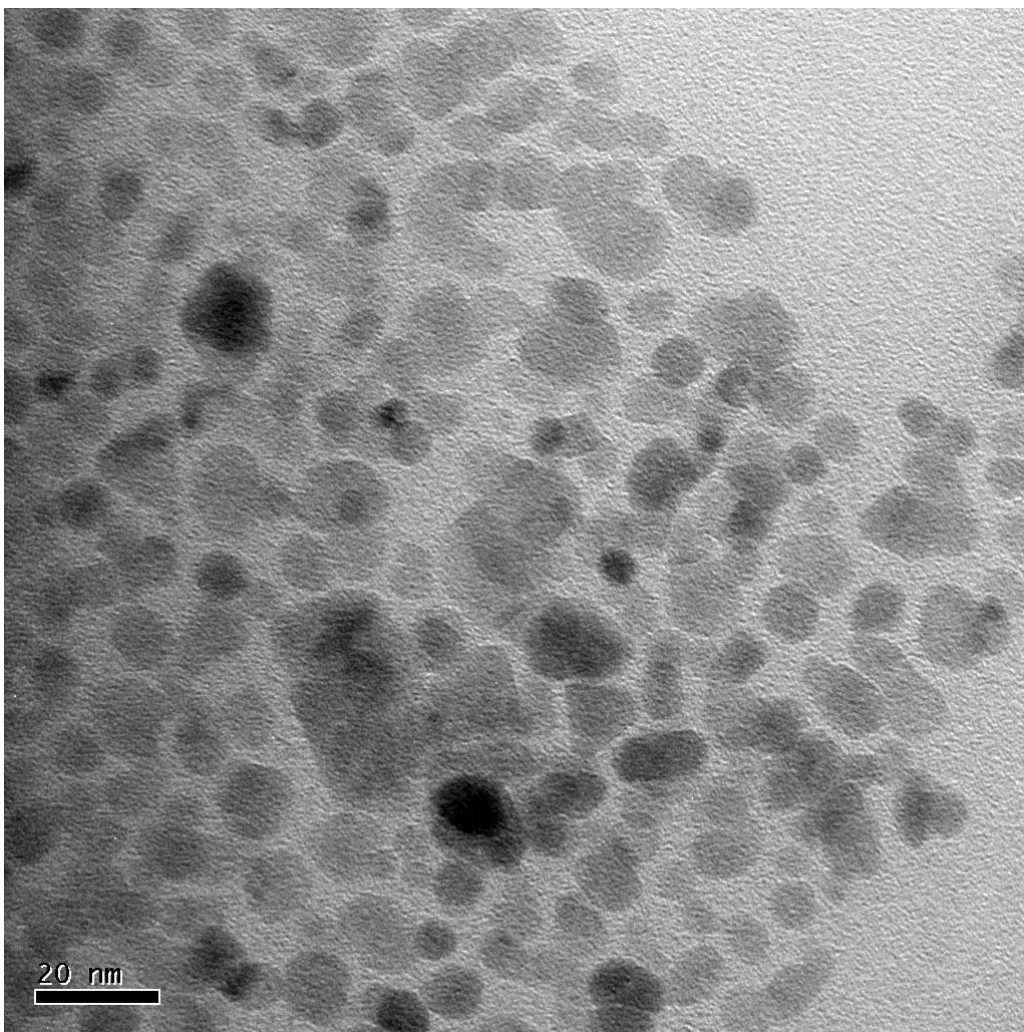


Figure 3-1. TEM micrograph of sample M1-3a-9.

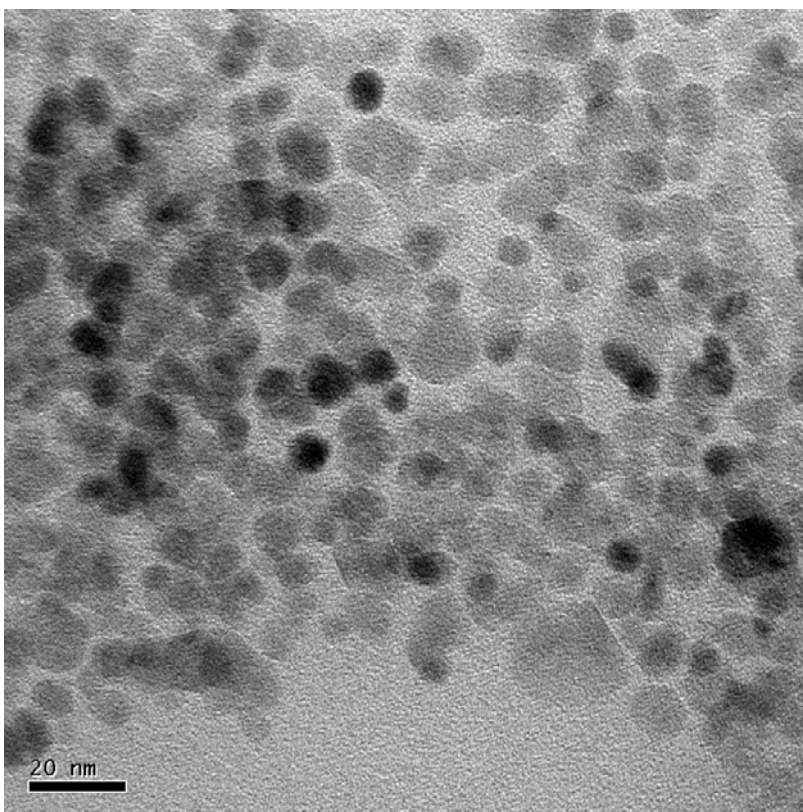


Figure 3-2. TEM micrograph of sample M1-3a-9.

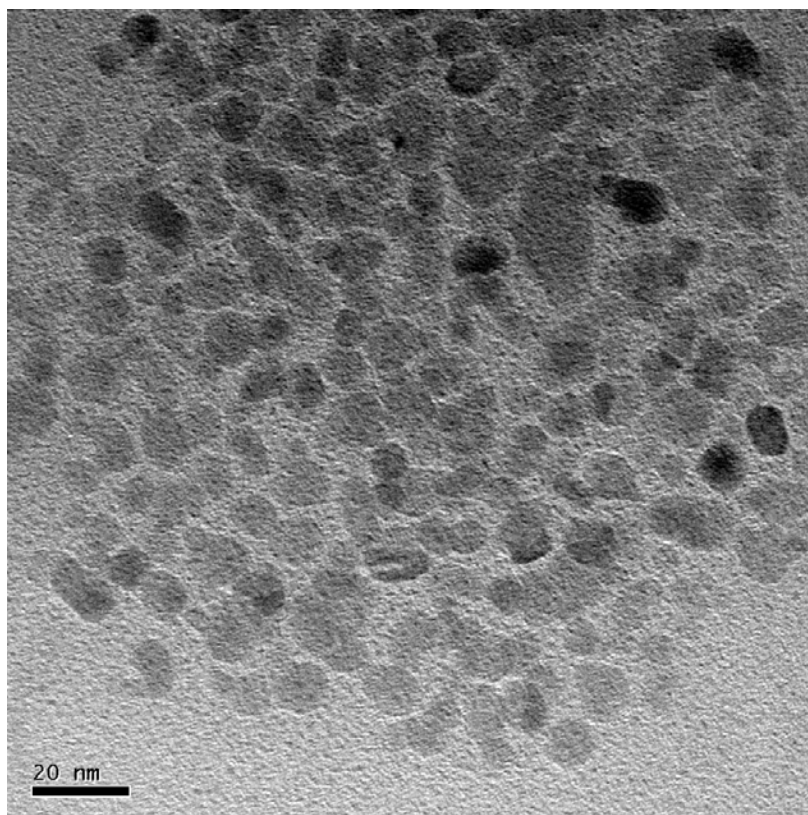


Figure 3-3. TEM micrograph of sample M1-3c-15.

Approximate size distributions of the M1-3 series of particles can be seen in the histograms shown in Figures 3-4 to 3-5. This data was then compared using a one-way ANOVA test, showing that samples M1-3a-9 and M1-3c-15 were not significantly different from each other ($P < 0.05$).

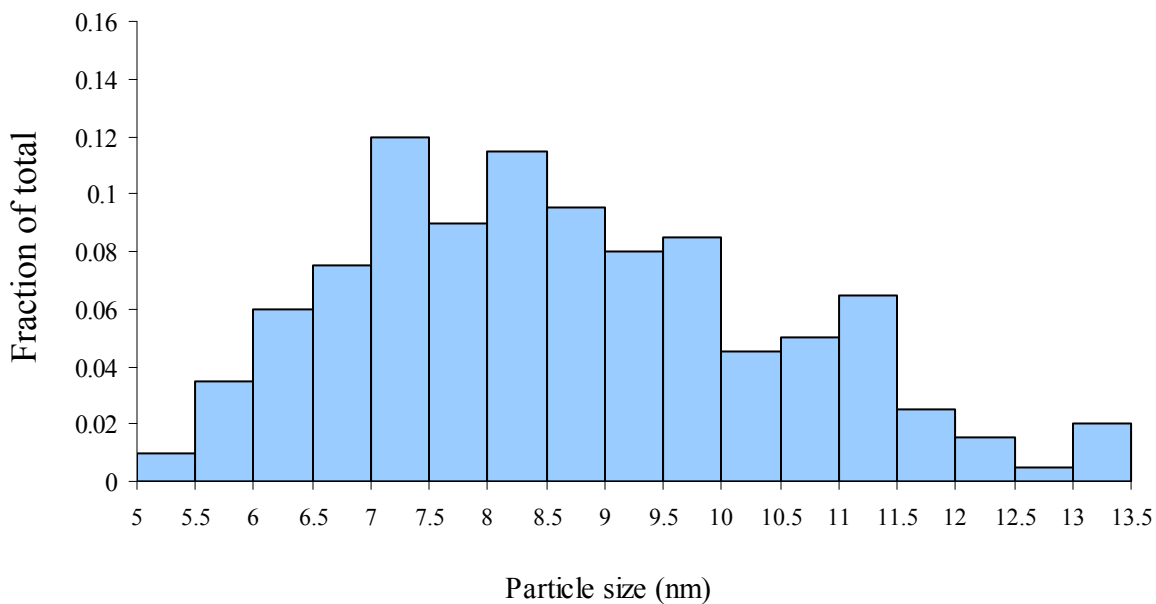


Figure 3-4. Particle size distribution for sample M1-3a-9.

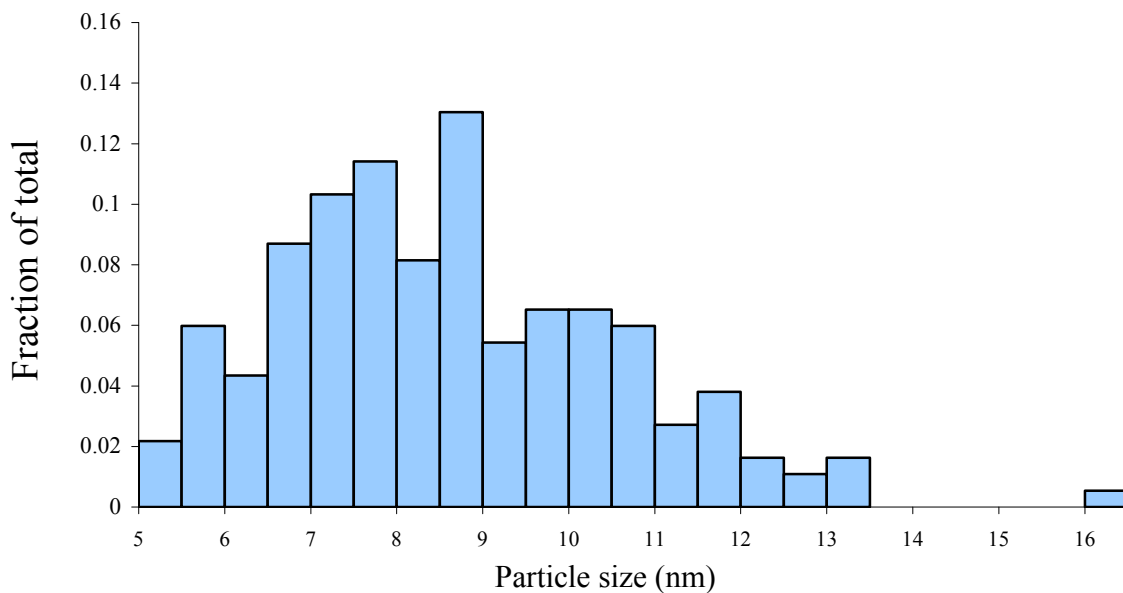


Figure 3-5. Particle size distribution for sample M1-3c-15.

Following this brief study, a more thorough literature search was done, showing that four primary variables were adjustable in the precipitation procedure: iron chloride concentration, reaction time, temperature, and stirring rate. Increasing both the iron chloride concentration and reaction time result in increased particle sizes whereas increasing the temperature and stirring rate result in decreased particle sizes. The next study was done in comparison to the existing M1-3 series, adjusting iron chloride concentration. Micrographs for M2 (decreased concentration as compared to M1) and M4 (increased concentration) are shown in Figures 3-6 to 3-8.

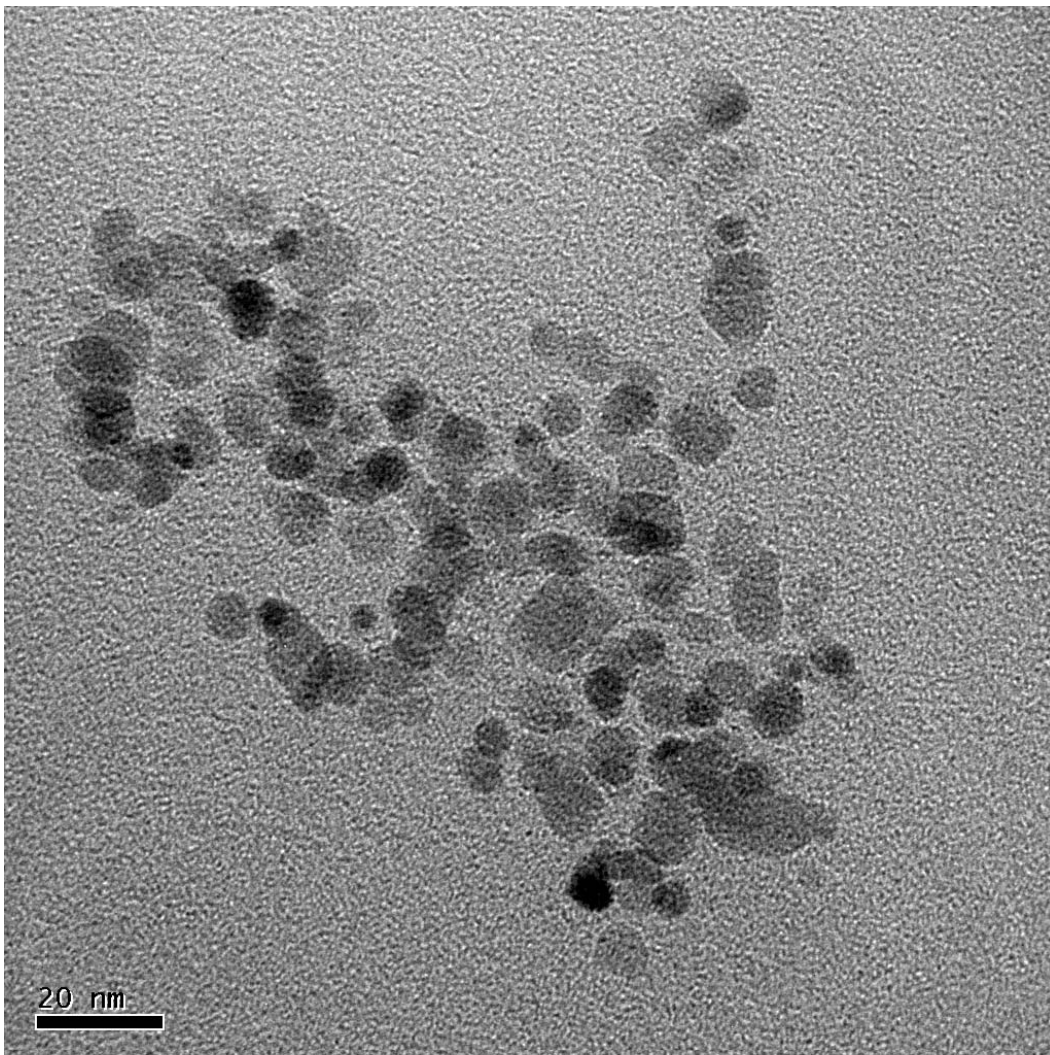


Figure 3-6. TEM micrograph of sample M2-3a-9.

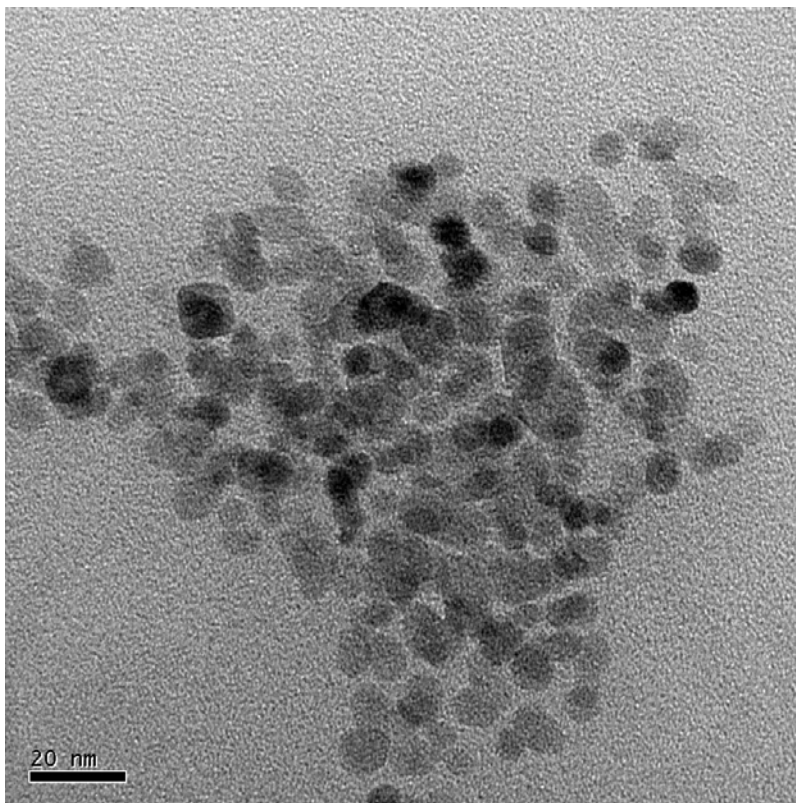


Figure 3-7. TEM micrograph of sample M2-3a-9.

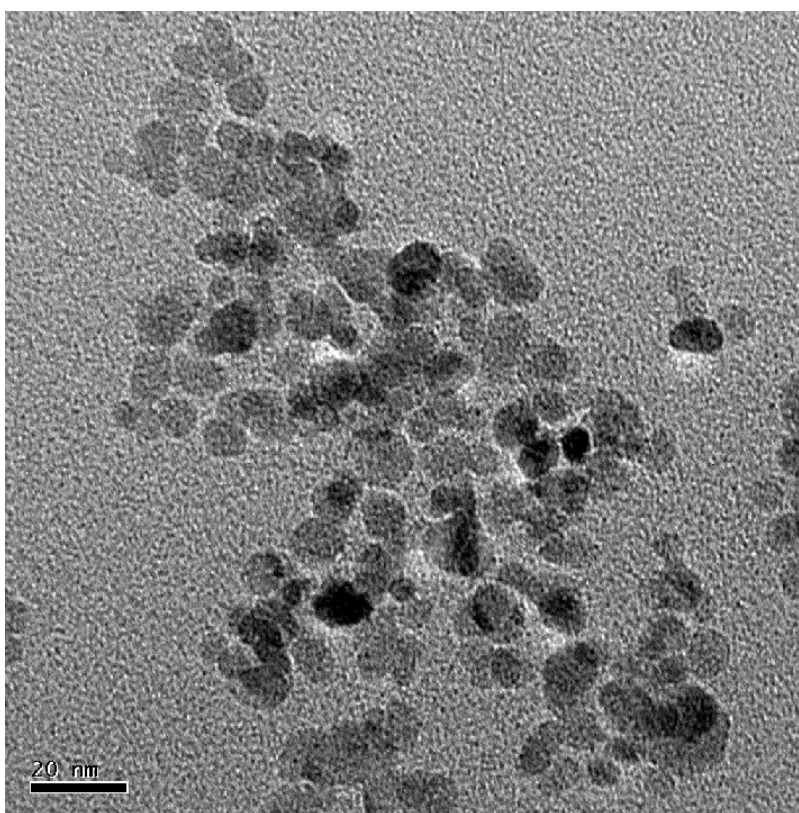


Figure 3-8. TEM micrograph of sample M4-4b-25.

Particle size distributions for samples M2-3a-9 and M4-4b-25 are shown in Figures 3-9 and 3-10. A summary of this data, along with M1-3a-9 for comparison, is shown in Figure 3-11. One-way ANOVA analysis showed that samples M1-3a-9 and M4-4b-25 are significantly bigger than M2-3a-9 but not significantly different compared to each other.

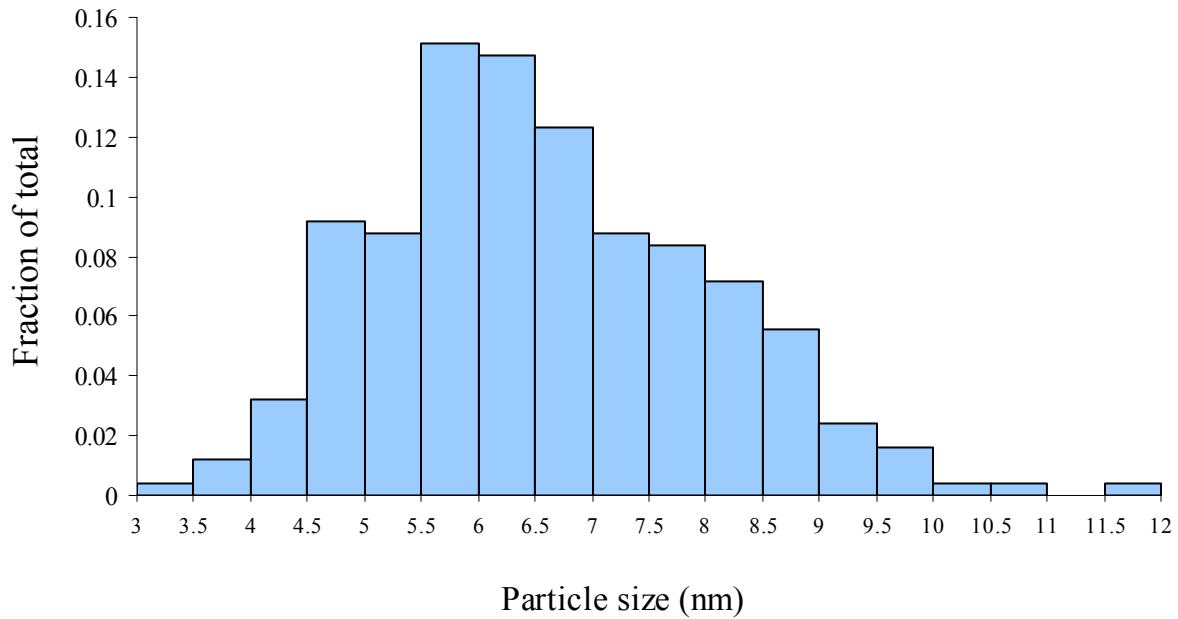


Figure 3-9. Particle size distribution for sample M2-3a-9.

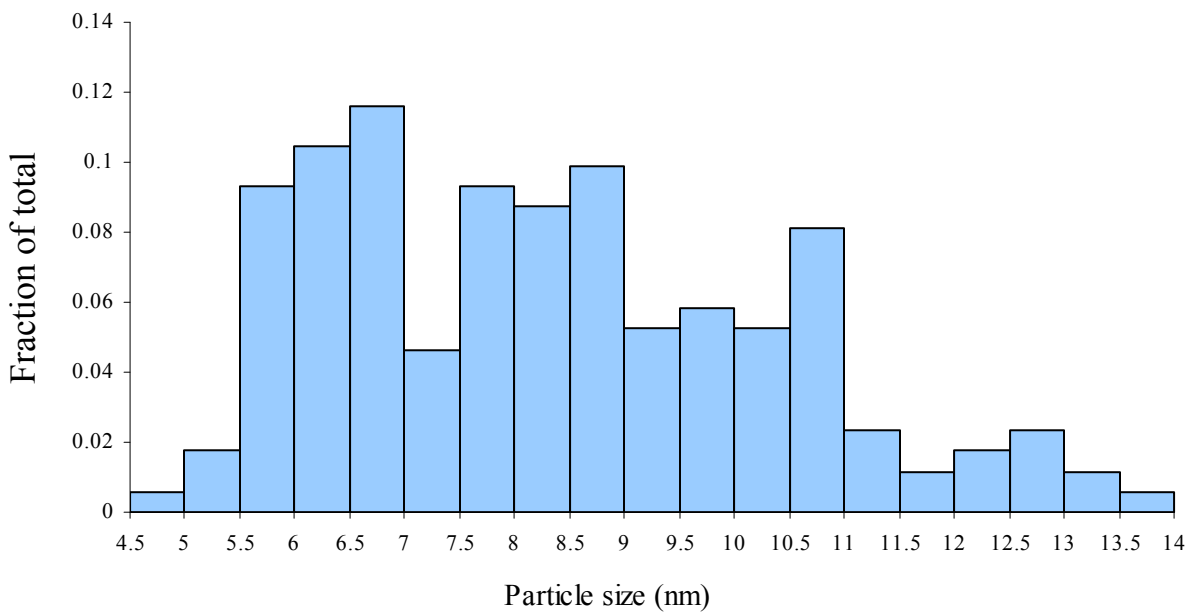


Figure 3-10. Particle size distribution for sample M4-4b-25.

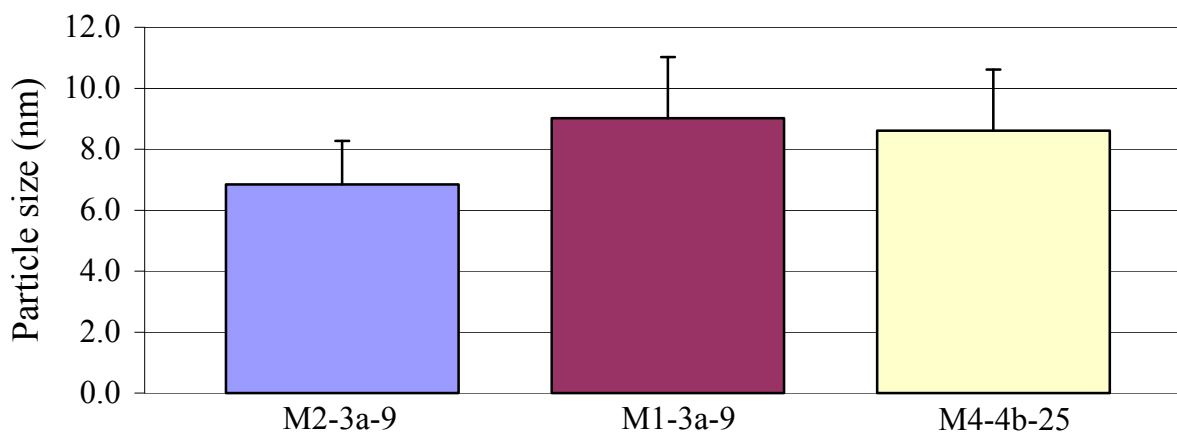


Figure 3-11. Comparison of mean particle sizes. Error bars show standard deviation.

Since these results were somewhat inconclusive and sizes beyond 10 nm were not produced, another study was performed examining reaction time. TEM analysis was not possible for all samples from this study as little to no particles were seen on the grids for samples M1-2g-20 and M1-2f-25. However, there was sufficient present for the remaining samples to allow some estimation of the effect of altering reaction time during precipitation. Examples of micrographs for the M1-2 series of particles are shown in Figures 3-12 to 3-15.

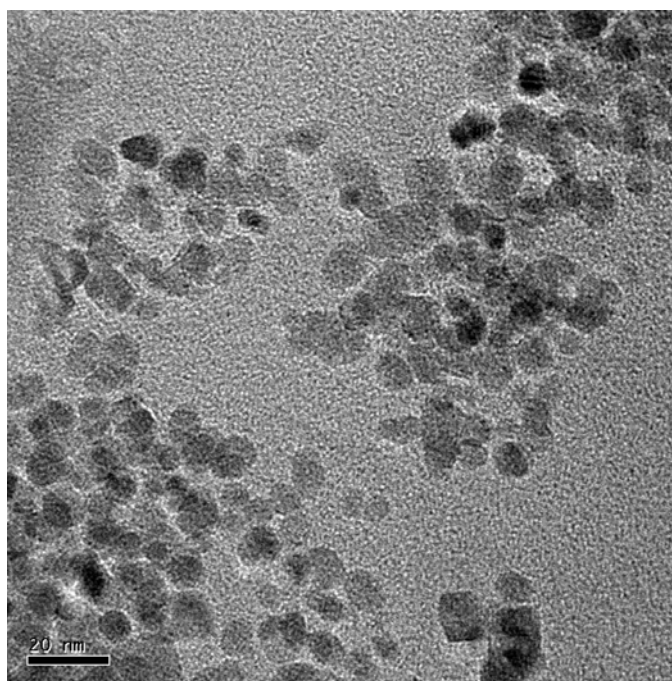


Figure 3-12. TEM micrograph of sample M1-2a-10.

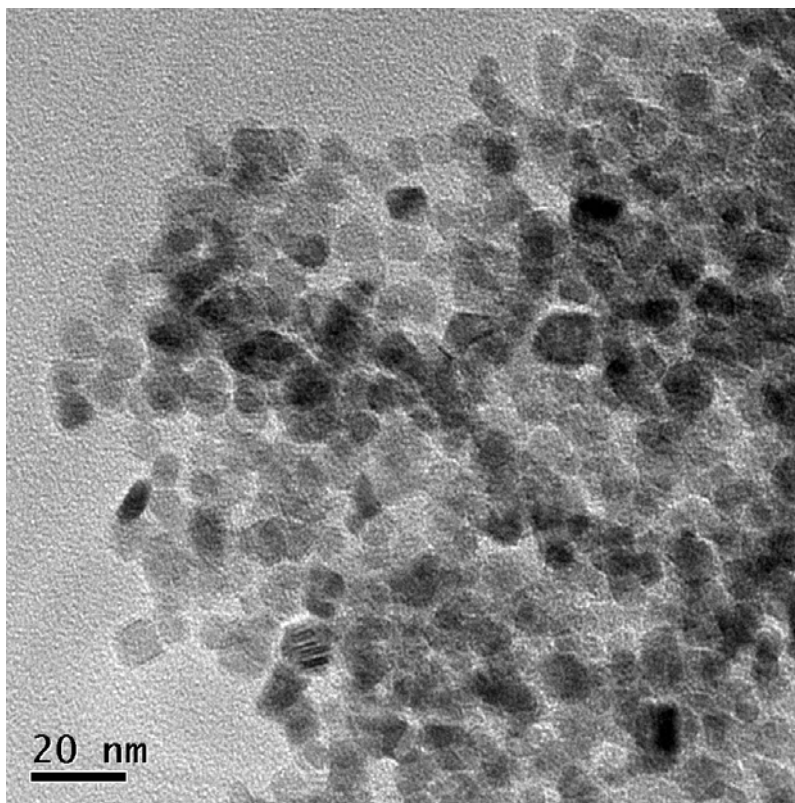


Figure 3-13. TEM micrograph of sample M1-2b-15.

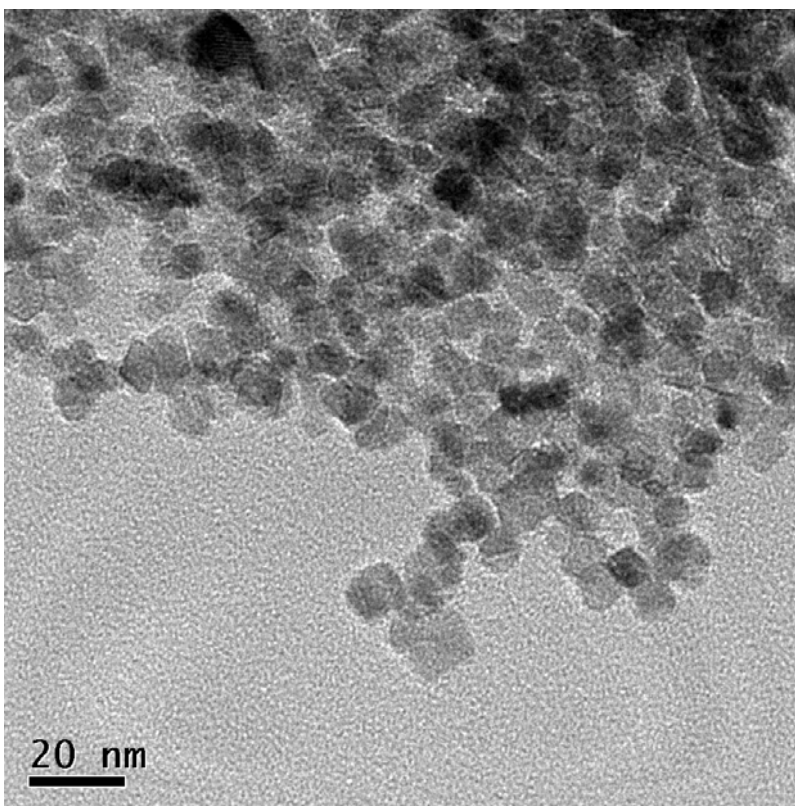


Figure 3-14. TEM micrograph of sample M1-2b-15.

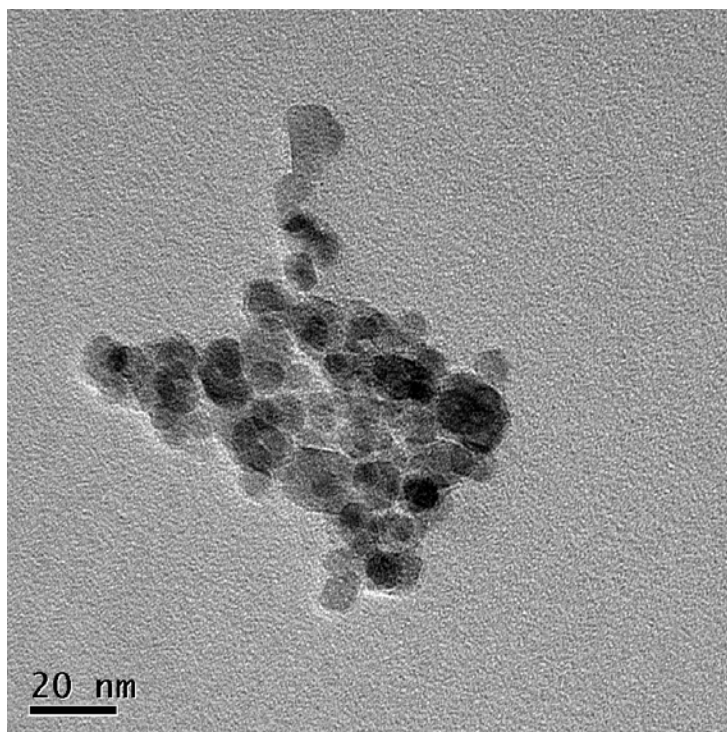


Figure 3-15. TEM micrograph of sample M1-2e-30.

Size distributions of the M1-2 series of particles can be seen in the histograms shown in Figures 3-16 to 3-18. A summary of these histograms is shown in Figure 3-19. These samples were again analyzed with a one-way ANOVA test, showing that samples M1-2b-15 and M1-2e-30 were significantly different from M1-2a-10 but not from each other ($P < 0.05$).

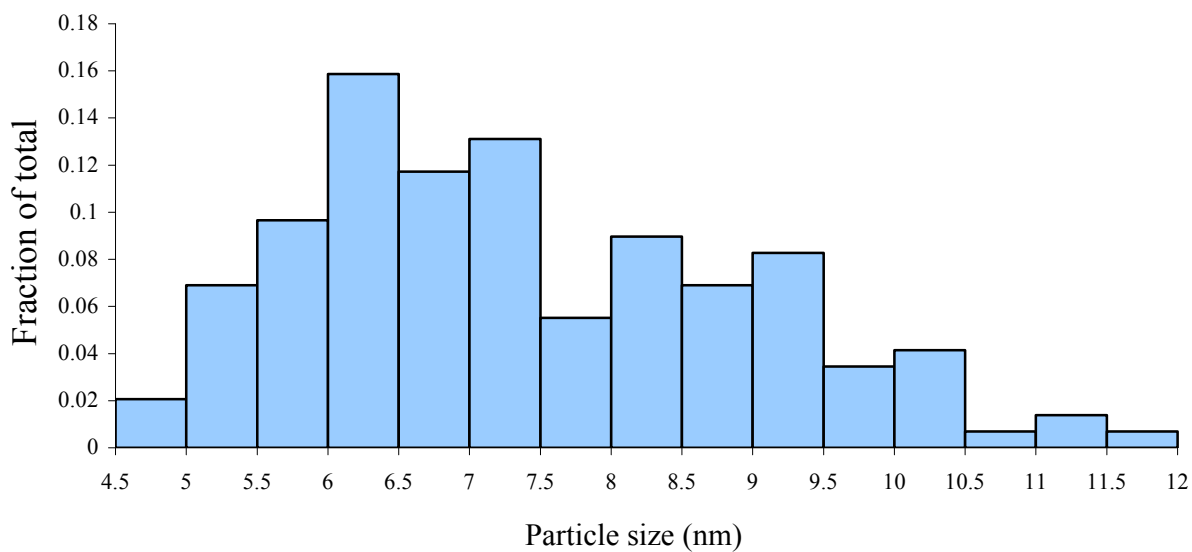


Figure 3-16. Particle size distribution for sample M1-2a-10.

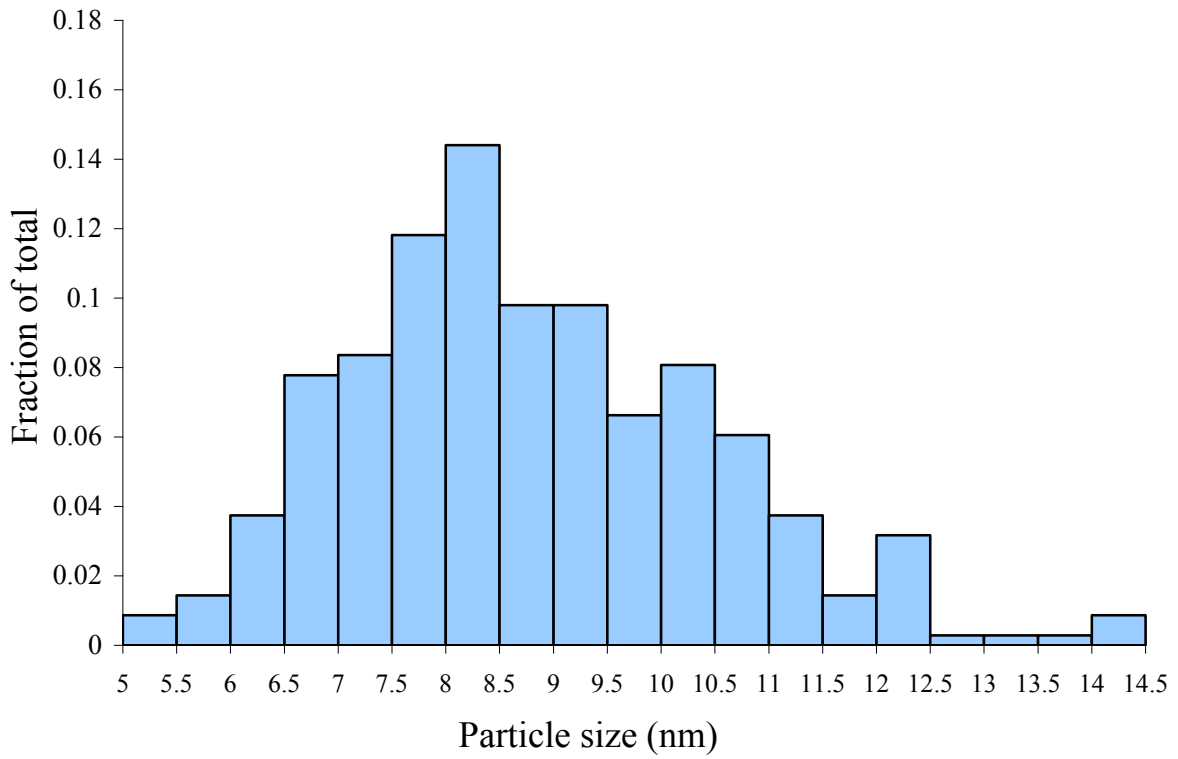


Figure 3-17. Particle size distribution for sample M1-2b-15.

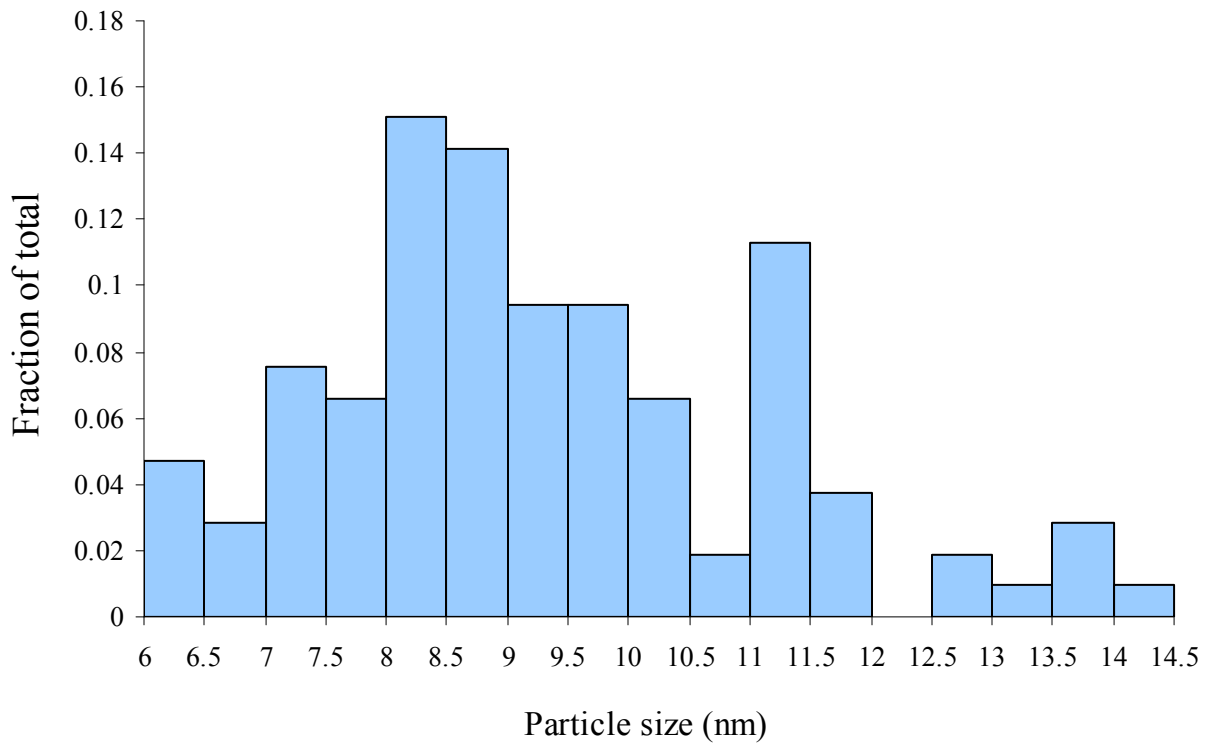


Figure 3-18. Particle size distribution for sample M1-2e-30.

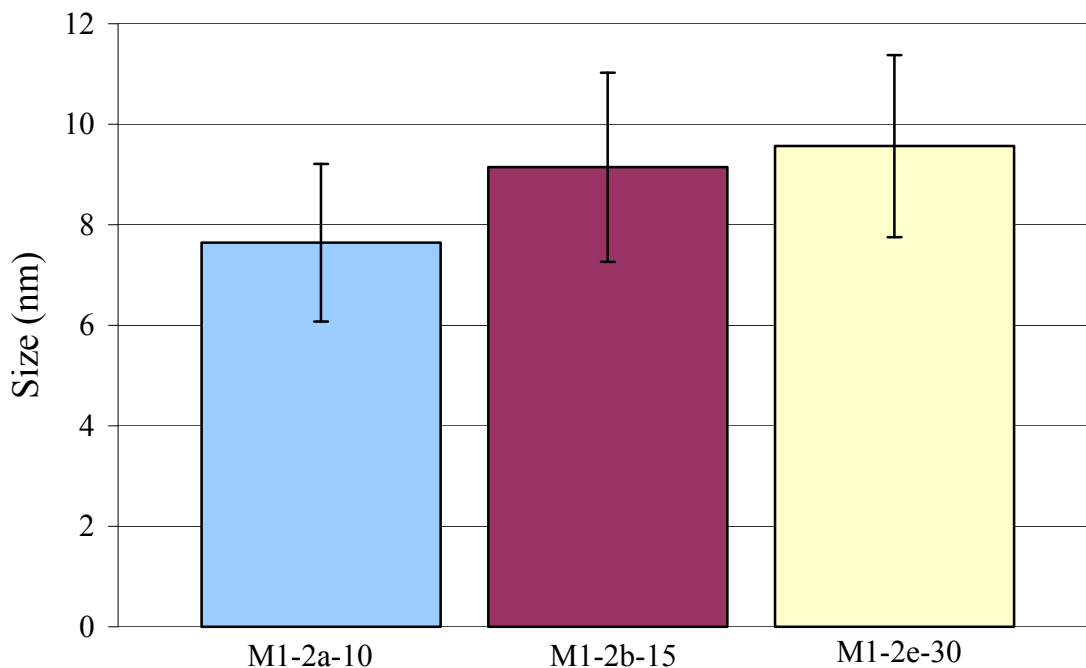


Figure 3-19. Comparison of mean particle sizes. Error bars represent the standard deviation.

Discussion

All of the TEM micrographs have a significant level of background noise. This is primarily due to the presence of oleic acid. The majority of the particles appear to be fairly well separated from others. There are certainly overlapping particles, seen as darker spots, but it does not appear as if there is significant particle agglomeration in some of the samples. There are some cases in which it is unclear if the individual particles are large, or they are some form of agglomerate. For all analysis, these particles were not measured so as not to skew the results artificially. Analysis of some of the distributions, however, would suggest that agglomeration may be playing a role in samples M1-2a-10 and M1-2e-30. This is most easily seen in M1-2e-30 with the significant increase in number of particles from 11 to 11.5 nm and then the small grouping from 12.5 to 14.5 nm. Further study of this data would be required to firmly establish whether agglomeration is occurring in these samples.

As can be seen from the results above, adjusting the timing of the addition of oleic acid had little effect in controlling particle size. While changing the concentration of iron chlorides did have a significant effect, these are not seen until relatively large changes are made, as seen between samples M2-3a-9 and M1-3a-9. However, a similar increase in concentration between M1-3a-9 and M4-4b-25 yielded statistically similar particle sizes. The results examining the effect of altering reaction time were also somewhat inconclusive. Evidently there is some effect as there was an increase in particle size between 10 minutes and 15, but beyond that it is unclear whether there is any further growth with time.

It is possible that the leveling off in particle size is partly due to settling before small samples were taken from each for dilution. Further study would be necessary to determine if this is the case.

X-Ray Absorption Near Edge Spectroscopy

As the XRD spectra gathered by Leamy for his PhD dissertation was inconclusive as to the phase of iron oxide produced, a more sensitive analysis technique was sought. Dr. Joanna Collingwood kindly volunteered to perform these tests while at the Diamond synchrotron facility in England. In addition to these samples, analysis was performed on iron foil so that that might be used as a control to compare the data to standards measured previously at the Materials Research Collaborative Access Team (MRCAT) Advanced Photon Source in Chicago.

Methods

Ferrofluid samples were diluted from 2 μL to 180 μL with double distilled water. Samples were then placed in a custom polycarbonate well plate, in which two sides and top of the wells were open. Kapton tape was placed to cover the sides of the wells yet allow the beam to pass through. Initially, the top of each well was left open. However, the first tests resulted in signal loss due to evaporation so as a result, kapton tape was also placed to cover the top of the wells.

All data analysis for these samples was performed using Athena, which is an EXAFS analysis program designed at the University of Chicago and built on the Ifeffit engine. First, a comparison was made between the two iron foil samples, run at MRCAT and Diamond. However, due to apparent oxidation of the Diamond sample, this was not suitable as a comparison for data between the two beam lines. Instead, a shift of -3.4 eV was made such that features such as the pre-K edge and other features in the curve matched with identifiable portions of the known standards.

Results

Estimations of the fractions of each oxide phase present were done by performing linear combination fits with Athena. First, each of the unknown samples were shifted by -3.4 eV as described above. Each of the curves for the unknown samples was then compared to the curves for magnetite, maghemite, goethite and hematite. Magnetite and maghemite are the primary phases expected, although goethite has been shown to be present if the acidity of the iron chloride solution is not low enough before addition of base [46]. Hematite is less prevalent in the literature, but the heavy weighting in the linear fits gives reason to believe it may well be present. The fits were plotted, along with the original data (designated μ), against known standards. The most likely fits were established by comparing the reduced chi squared values, which are shown in Figures 3-20 to 3-25. More detailed information about each fit, including the chi squared values and compositions, is shown following each figure in Tables 3-3 to 3-8.

Table 3-3. Linear combination fit for XANES data from sample M1-3b-9, sorted by chi squared.

Chi squared	Fraction of Magnetite	Maghemite	Goethite	Hematite
0.110	0.43	0.35	0.22	0
0.145	0.45	0.55	0	0
0.193	0.51	0	0.49	0
0.218	0.39	0.22	0.39	0
0.254	0.44	0	0.56	0
0.341	0.41	0.59	0	0

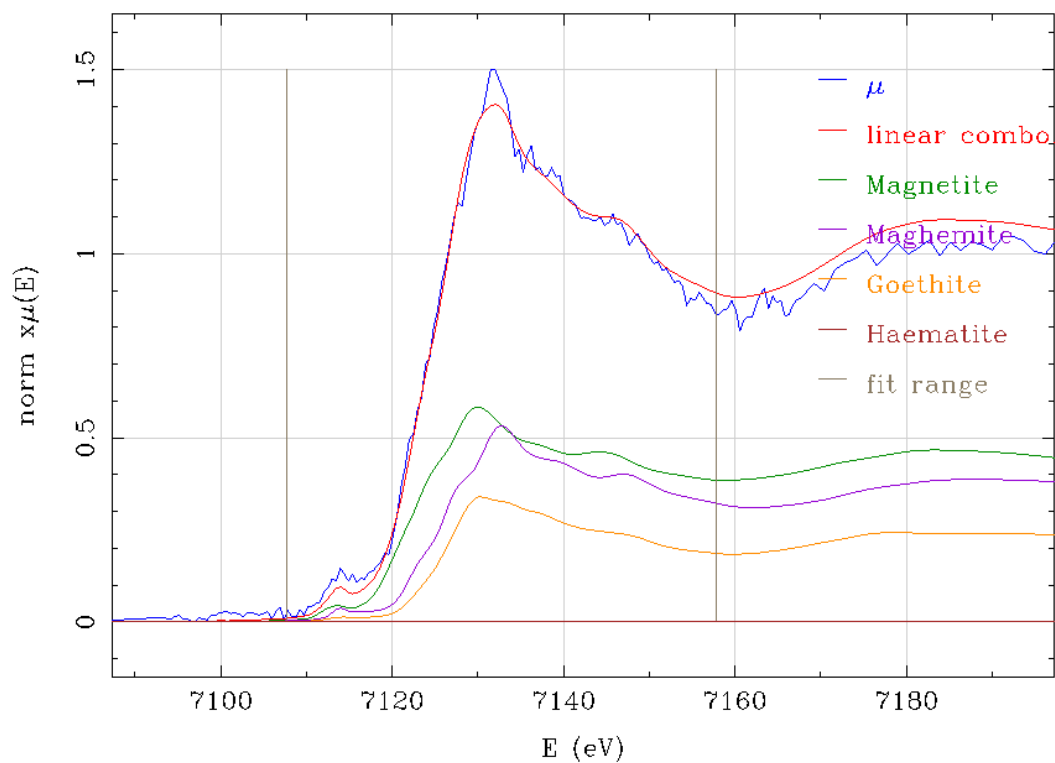


Figure 3-20. Linear combination fit for XANES data from sample M1-3b-9.

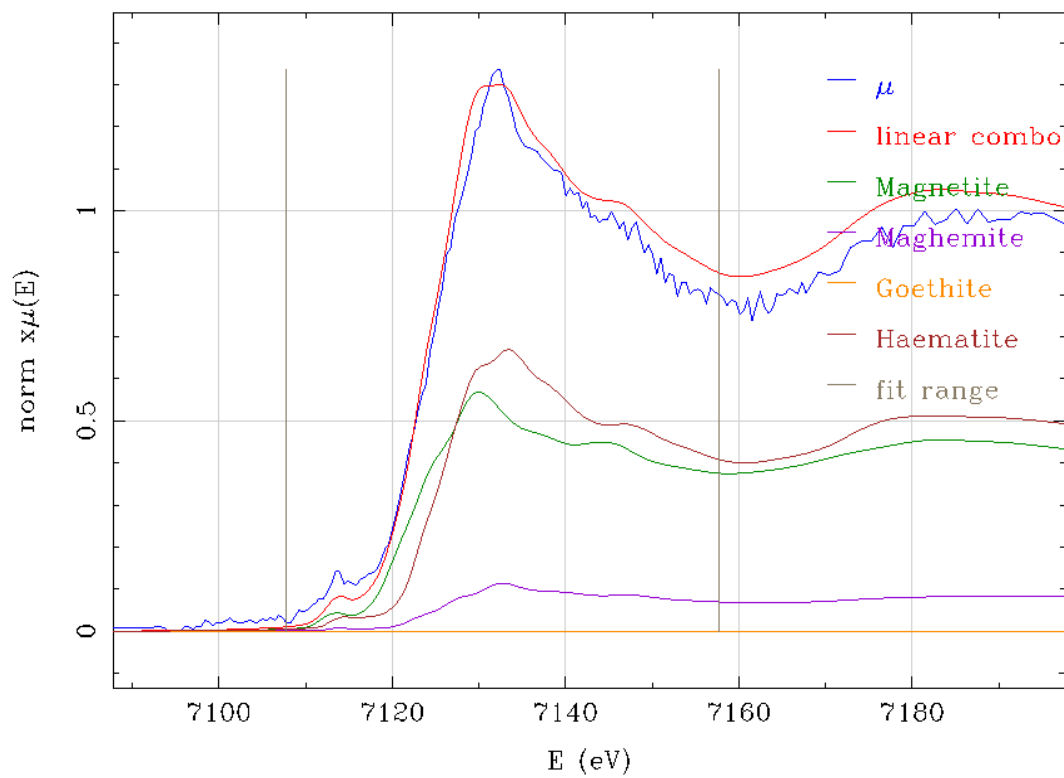


Figure 3-21. Linear combination fit for XANES data from sample M2-4a-9.

Table 3-4. Linear combination fit for XANES data from sample M2-4a-9, sorted by chi squared.

Chi squared	Fraction of Magnetite	Maghemite	Goethite	Hematite
0.286	0.43	0.08	0	0.49
0.287	0.43	0	0	0.57
0.337	0.49	0.51	0	0
0.339	0.46	0.54	0	0

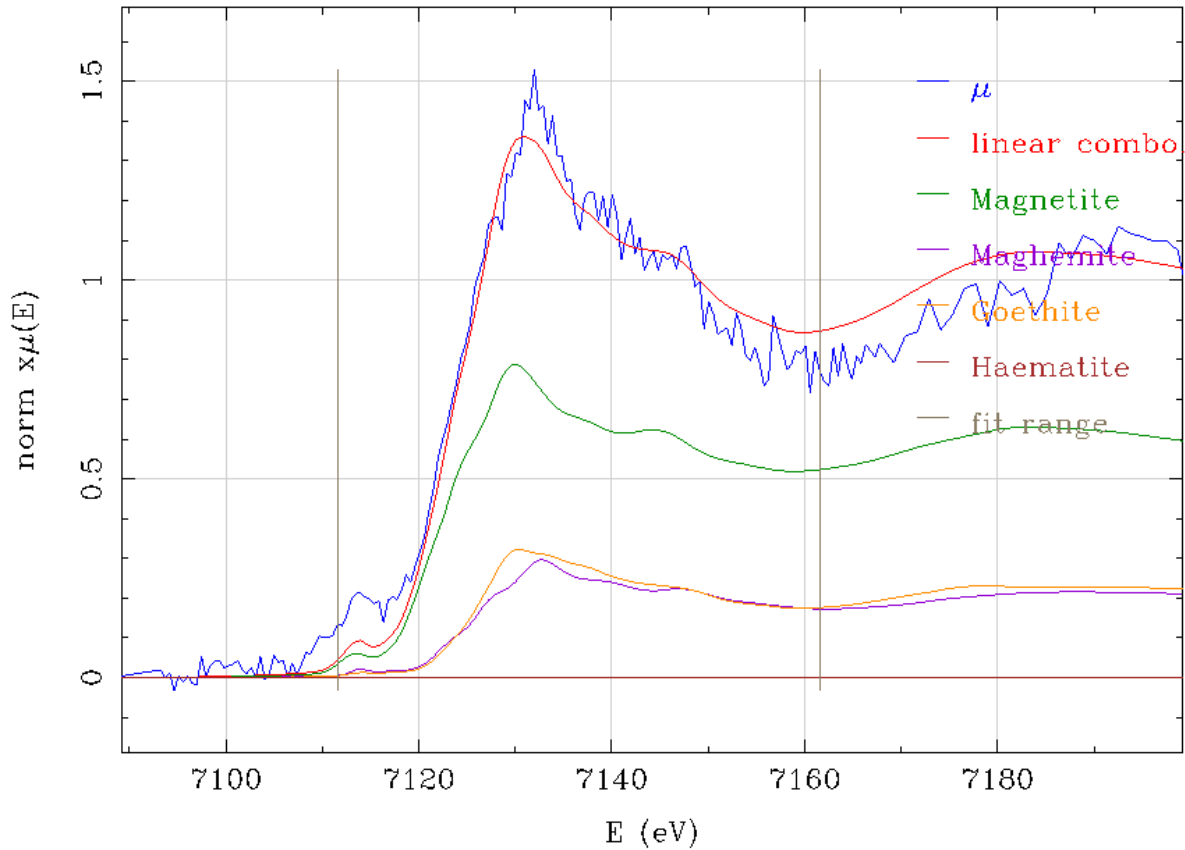


Figure 3-22. Linear combination fit for XANES data from sample M1-3a-9.

Table 3-5. Linear combination fit for XANES data from sample M1-3a-9, sorted by chi squared.

Chi squared	Fraction of Magnetite	Maghemite	Goethite	Hematite
0.526	0.61	0.25	0.14	0
0.542	0.62	0.38	0	0
0.567	0.65	0	0.35	0
0.579	0.58	0.16	0.26	0
0.596	0.62	0	0.38	0
0.636	0.60	0.40	0	0

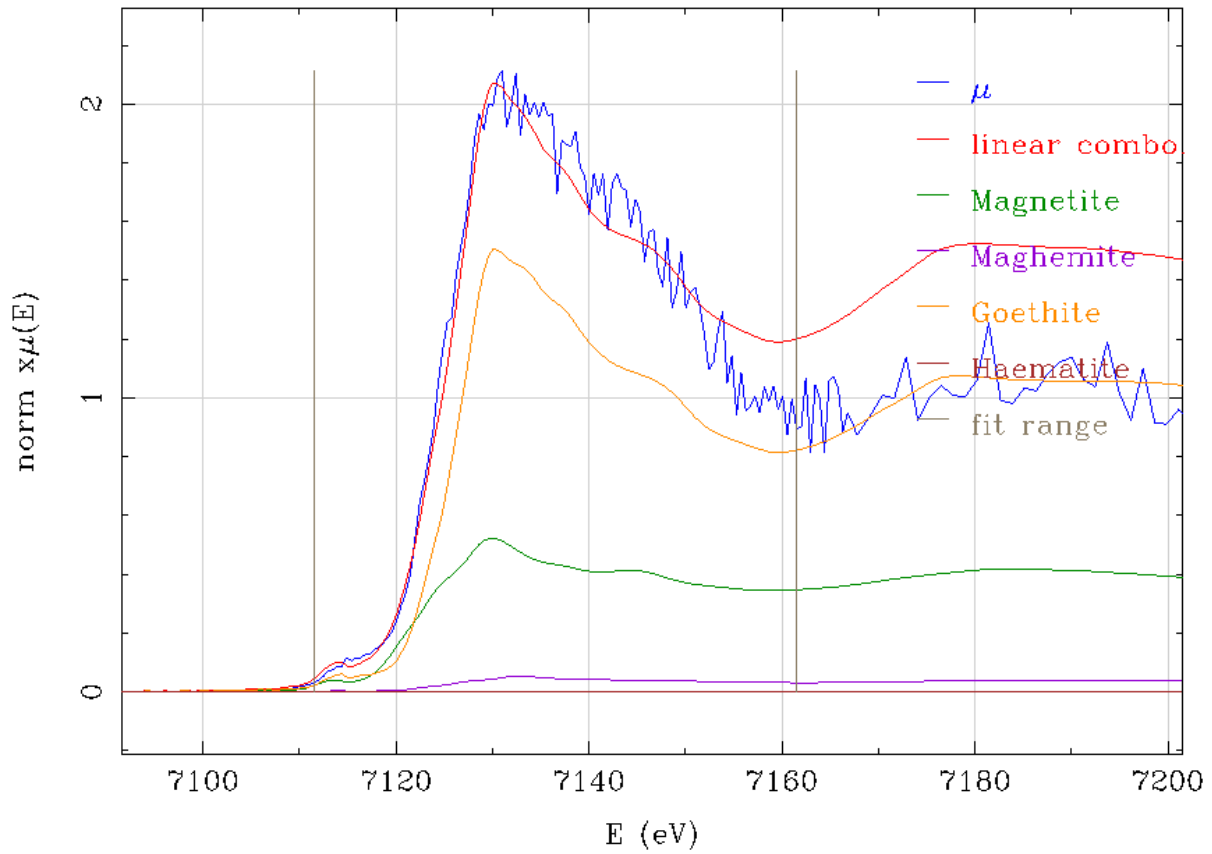


Figure 3-23. Linear combination fit for XANES data from sample M1-3c-15.

Table 3-6. Linear combination fit for XANES data from sample M1-3c-15, sorted by chi squared.

Chi squared	Fraction of Magnetite	Maghemite	Goethite	Hematite
1.505	0.27	0.03	0.70	0
1.509	0.30	0	0.70	0
1.871	0	0.30	0.70	0
2.867	0.32	0.68	0	0
18.21	0	0	1	0

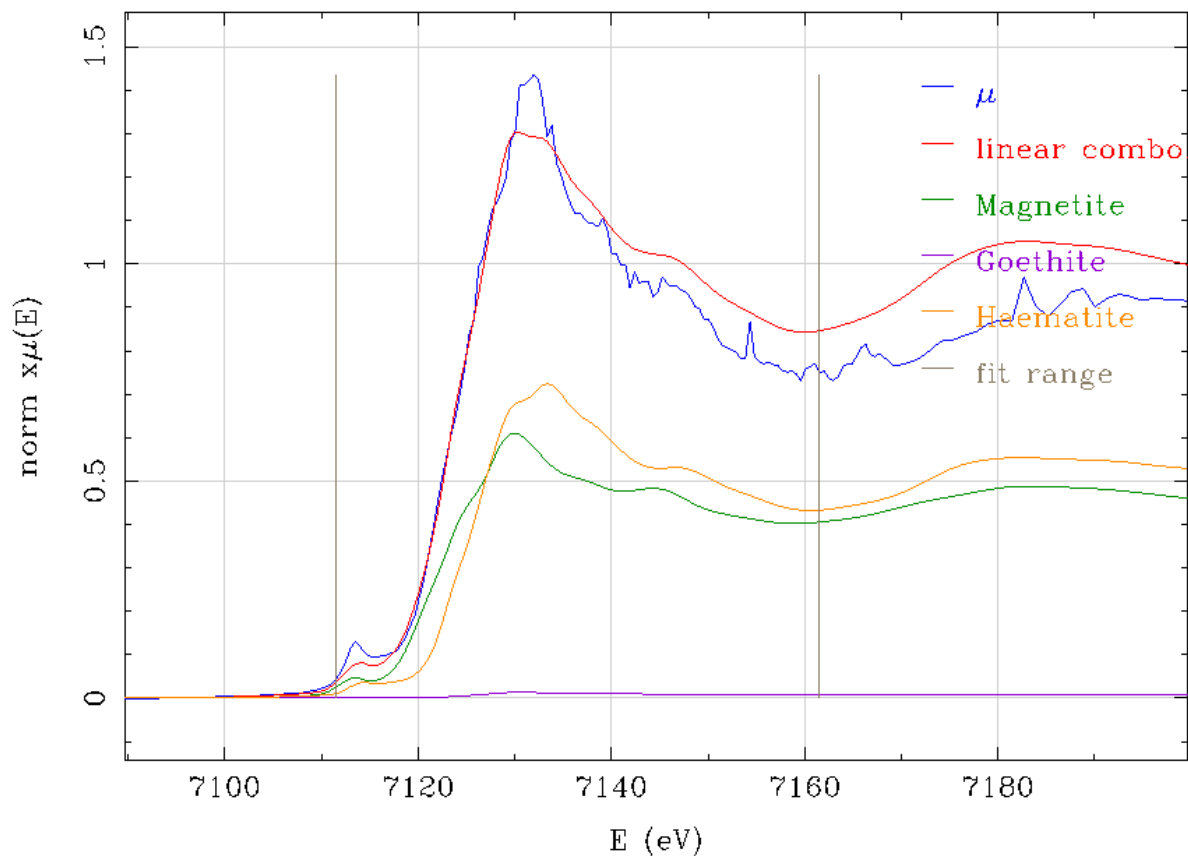


Figure 3-24. Linear combination fit for XANES data from sample M2-3a-9.

Table 3-7. Linear combination fit for XANES data from sample M2-4a-9, sorted by chi squared.

Chi squared	Fraction of Magnetite	Maghemite	Goethite	Hematite
0.464	0.47	0	0	0.53
0.549	0.56	0.14	0.30	0
0.562	0.59	0	0.41	0

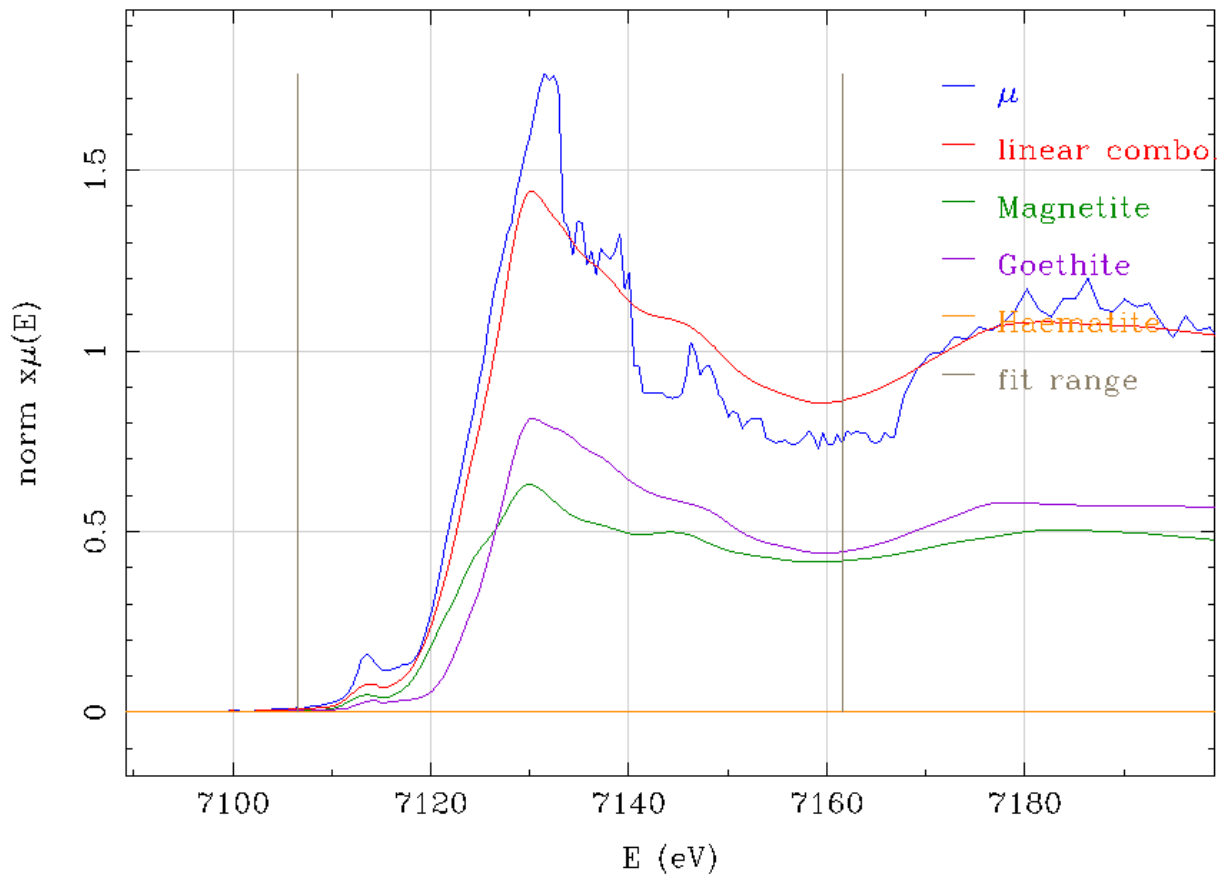


Figure 3-25. Linear combination fit for XANES data from sample M4-4b-25.

Table 3-8. Linear combination fit for XANES data from sample M4-4b-25, sorted by chi squared.

Chi squared	Fraction of Magnetite	Maghemite	Goethite	Hematite
2.033	0.48	0	0.54	0
2.067	0.44	0	0.56	0
2.616	0.56	0	0	0.44

Discussion

As shown by the high chi squared values, these fits are far from exact. The large amount of noise in each of the original data curves certainly does not help. Nor does the lack of certainty that the E_0 values, where the edge begins, are calibrated correctly. However, various elements in each curve are characteristic of certain phases. Since magnetite or maghemite is expected, pre-K edge peaks can be matched to those to some degree. Also, the location of the shoulder at

approximately 7145 to 7150 eV gives a great deal of information as to which phases might be present.

While these results are far from exact, they do provide more of an insight than is generally known about what oxides are present. As a result, more is now understood about the adjustment necessary to the precipitation protocol in order to maximize the heating ability of the system. Specifically, the presence of goethite indicates that the iron chloride solution should in all likelihood be more acidic before reacting with ammonium hydroxide. Goethite is only weakly magnetic, so if this can be corrected, the quantities of magnetite or maghemite may be increased, allowing higher rates of heating.

The presence, or lack thereof, of hematite could be established by analyzing the particles once again with XRD. While the exact quantities of the phases could not be calculated, this would allow for re-examination of the XANES data if hematite were shown to certainly not be present.

Superconducting Quantum Interference Device (SQUID) Magnetometry

SQUID magnetometry is one of the most sensitive methods of measuring extremely small magnetic fields. A Quantum Design SQUID magnetometer was used to measure the hysteresis curves for bare magnetite and oleic acid-coated magnetite samples. All sample preparation and testing was performed by Leamy for his PhD dissertation [43]. This data is reproduced here due to the similar preparation methods and size of the particles: 10.6 +/- 0.8 nm for Leamy's particles. As such, the shape of the hysteresis curve should accurately represent that of the currently employed particles. However, the phase of these particles may differ slightly from those currently produced. As such the magnitude of the magnetization reported may not be accurate.

Methods

Briefly, bare magnetite was prepared as described above at room temperature with a reaction time of ten minutes and without oleic acid. Following precipitation, the oxide was centrifuged and washed three times. The oxide was redispersed using a vortexer and sonic bath. Finally, the oxide was centrifuged once more and freeze dried overnight.

Oleic acid-coated particles were prepared identically to the bare magnetite, except that after the initial reaction, oleic acid in cyclohexane was added, coating the particles and drawing them into the cyclohexane. The cyclohexane ferrofluids was dried overnight, and then the oxide resuspended in chloroform, which was employed for making oxide-loaded PLGA microspheres. The chloroform ferrofluid was dried overnight before testing.

Results

Results for the SQUID magnetometry test are shown in Figure 3-26.

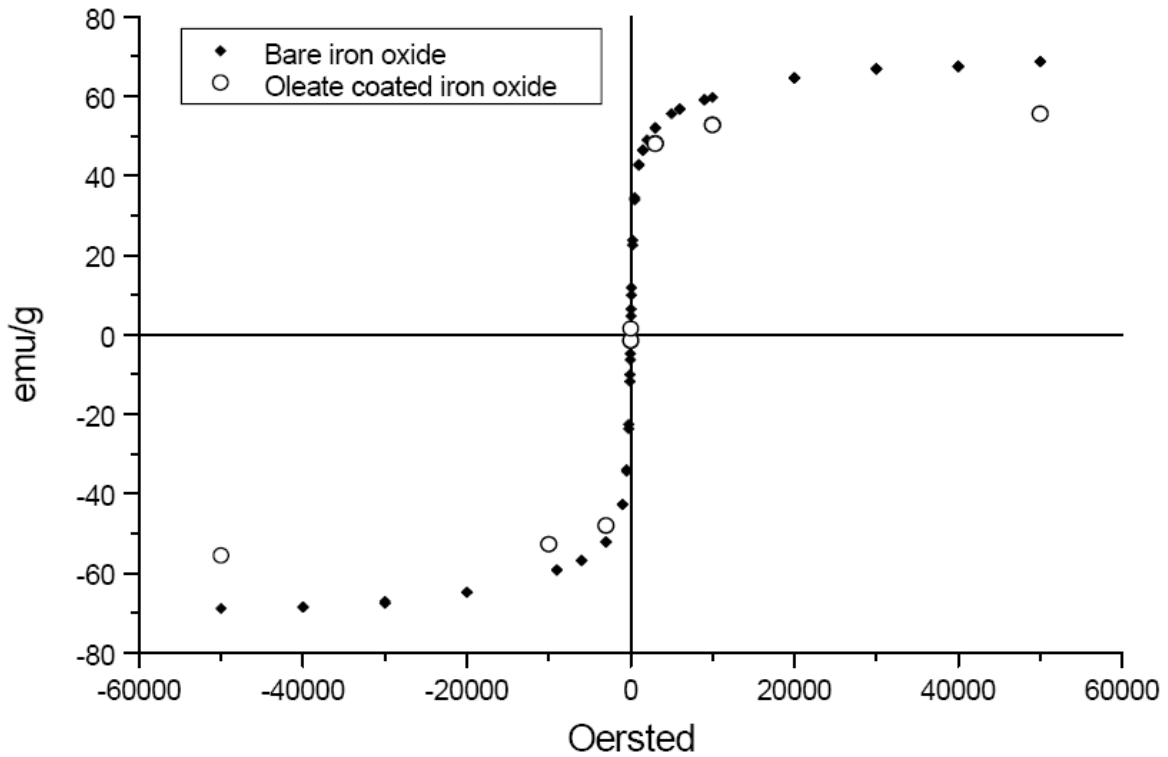


Figure 3-26. Hysteresis curves for iron oxides. Reproduced from Leamy, Figure 3-7 [43].

Discussion

As can be seen in Figure 3-25, there is almost no area within the curve, meaning there is negligible hysteresis. Considering this, and the size measured by examination of the TEM micrographs, the particles can definitively be called superparamagnetic. Because the particles used in that study were larger than those used in the study presented here, those for the current study should have similar magnetic properties. As such, repetition of the SQUID magnetometry test was deemed unnecessary in this case.

CHAPTER 4 HEATING OF FERROFLUIDS IN A MAGNETIC COIL

Resonant Circuits

There are several reasons for using a resonant circuit for magnetic hyperthermia applications: first, it provides an inductor, which is capable of inducing a homogeneous magnetic field that will actually be used for the test itself; secondly, it amplifies the current through the inductor in a very narrow range of frequencies, which means when optimized, the system will generate strong magnetic fields and be highly effective with a certain size of magnetic particles.

This resonance is generated by placing a capacitor (or group of capacitors) in parallel with the inductor. All of these components store energy: the capacitors in the form of a charge, and the inductor in magnetic energy. Due to the 180° phase lag between these two components, externally measured impedance of the circuit is high at all frequencies except in a small band [47]. The frequency at which this occurs is dependent on the storage capacities of the inductor and capacitor(s). At the center of this frequency range is the resonant frequency, at which the impedance for the circuit is minimized. Assuming the circuit is impedance matched with the source, little power is reflected back to the source. In this case, high current flows in either the capacitor or inductor while potential builds in the other. When this current flows through the inductor, relatively large magnetic fields are generated considering the magnitude of the generated signal.

Design of the Magnetic Coil

The magnetic coil in use for this study was first designed by a former graduate student of this research group, Dr. Albina Mikhaylova. This coil has a length of 100 mm, diameter of 53 mm and 55 turns, which yields an inductance of $58 \mu\text{H}$. The coil was originally designed for use at approximately 1 MHz, the coil being in parallel with a 330 pF capacitor. Since this is not

ideal for use with hyperthermia, an attempt was made first to redesign the coil for use at 100 kHz. Being impractical to alter the inductor—the magnetic coil—the decision was made to change the value of the capacitors parallel to the coil. For this, two $0.01\ \mu\text{F}$ capacitors were placed in parallel with each other, together being in parallel with the coil.

However, with the amplifiers on hand no resonance was seen in the vicinity of 100 kHz after making these changes. As a result, the capacitors were changed once again, this time putting them in series instead of in parallel. Since capacitors add inversely, this caused a shift in the theoretical resonant frequency to approximately 295 kHz. A schematic diagram of this coil circuit is shown in Figure 4-1, and a picture of the physical coil is shown in Figure 4-2.

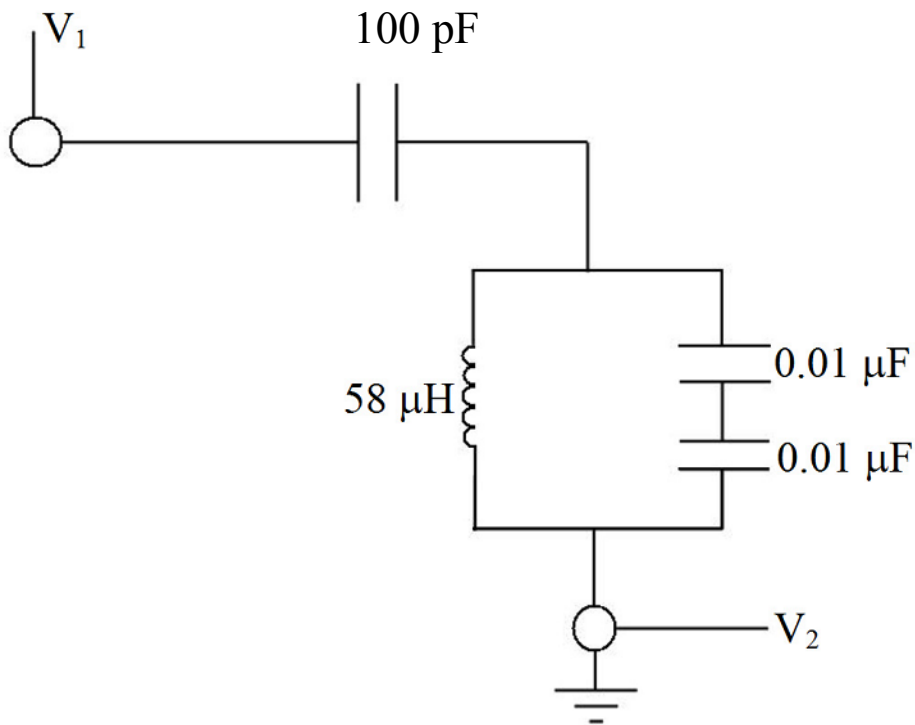


Figure 4-1. Schematic diagram of the coil circuit used during the study.

From this point, an analysis of the power reflected back to the amplifier was made, and found to have a minimum at approximately 285 kHz. This was further confirmed by attempting to heat particles in the coil and observing the point at which the maximum rate of heating occurred.

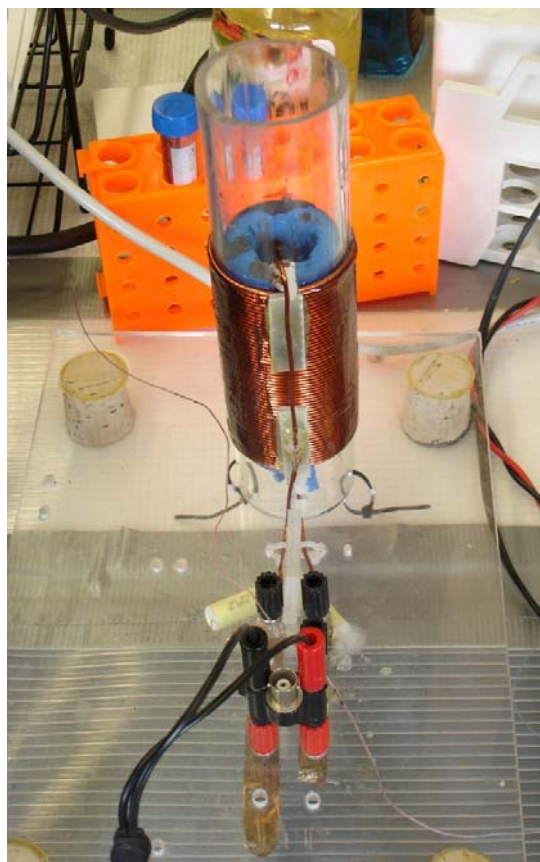


Figure 4-2. Image of the physical coil and connections.

Temperature Response of Ferrofluids

Since previous attempts at measuring the heating response of MCX-3 and MCX-4 series resulted in little heating in comparison to early attempts with the MC1-2 series, it was decided to continue with the use of the MC1-2 series for the remainder of this study. Evaluation of the size of the particles in MCX-3 and MCX-4 showed that the sizes were not readily controlled by altering the timing of addition of oleic acid during precipitation. A comparison of the analysis from the TEM data on these samples led to the hypothesis that these particles were too small for the χ'' to be maximized. Adjusting the concentration of iron chlorides may have been an option as this did seem to have a positive effect on the particle size, but to increase the size by any significant margin an extremely high concentration would have been necessary. As such, in

order to control the size of the particles for this study, the reaction time was altered. The size distributions for these particles are shown in Figures 3-14 and 3-15.

Methods

For testing, the desired signal was generated by a Pragmatic 2416A function generator, delivering a sin wave signal at 9 V output. This signal was then amplified using a Krohn-Hite 7602M wideband amplifier to approximately 75 W.

All the ferrofluids were kept in stable suspension, except where noted, by rotating in a hybridization incubator between runs. As the coil heats up significantly during these tests, a control was established, testing calcium phosphate in canola oil at the same concentration as the ferrofluids. Sample concentrations for both ferrofluids and the control were maintained at approximately 50 mg/mL. Temperature measurements were taken every 30 seconds using a thermocouple attached to an Omega HH506R thermometer.

The magnetic field strength was measured using a F. W. Bell model 5080 Gauss/Tesla meter. At the center of the coil it was homogeneous, with a strength of approximately 1.05 kA/m. The strength of the field decreased dramatically at the entrance to approximately 0.35 kA/m. Taking note of the field strength and frequency, $H \cdot f = 3.0 \times 10^8$ A/(m s), slightly over half the established safe limit of 4.85×10^8 A/(m s).

Results

Figure 4-3 shows the temperature response of the individual ferrofluids and the control, as a function of time. As the room temperature for each sample, and often individual runs, was not stable, these are plotted as a function of ΔT from room temperature rather than actual temperature. These results appear to be accurate regardless of the initial temperature. All error bars represent the standard deviation. Figure 4-4 shows the heating of the samples after subtracting the heating seen in the control sample, treating that as background heating.

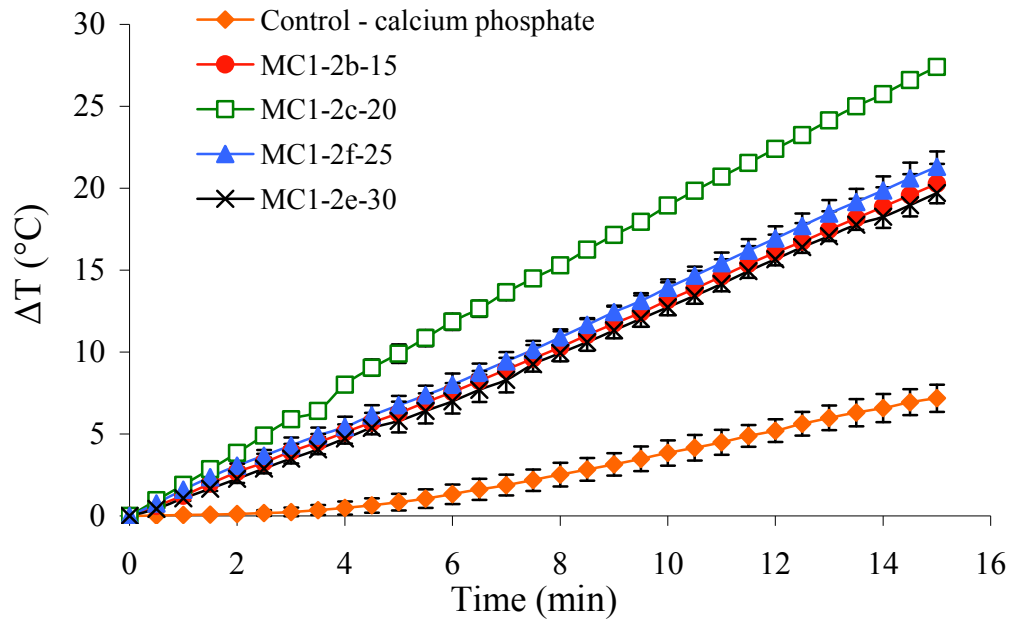


Figure 4-3. Heating of oil-based ferrofluids as a function of time. Concentration of ferrofluids was 50 mg/mL canola oil.

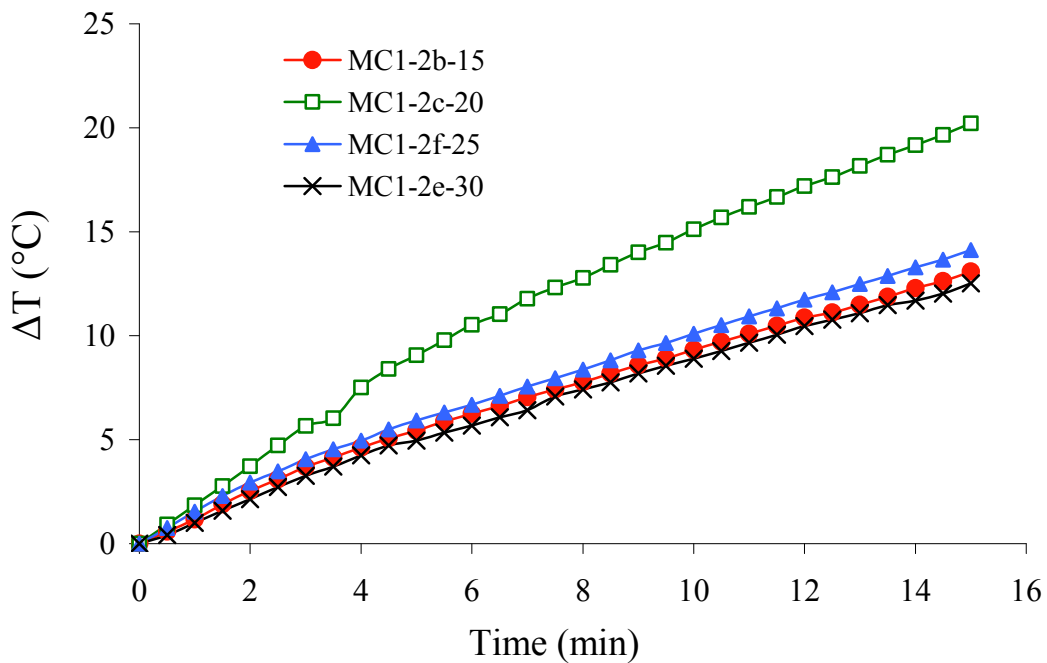


Figure 4-4. Heating of oil-based ferrofluids subtracting control heating.

The heating rates for each individual sample were relatively stable over time, which can be seen in the relatively linear nature of the curves. Due to this, the mean heating rates are reported rather than plotting the heating rates over time. The mean rates are shown in Figure 4-5.

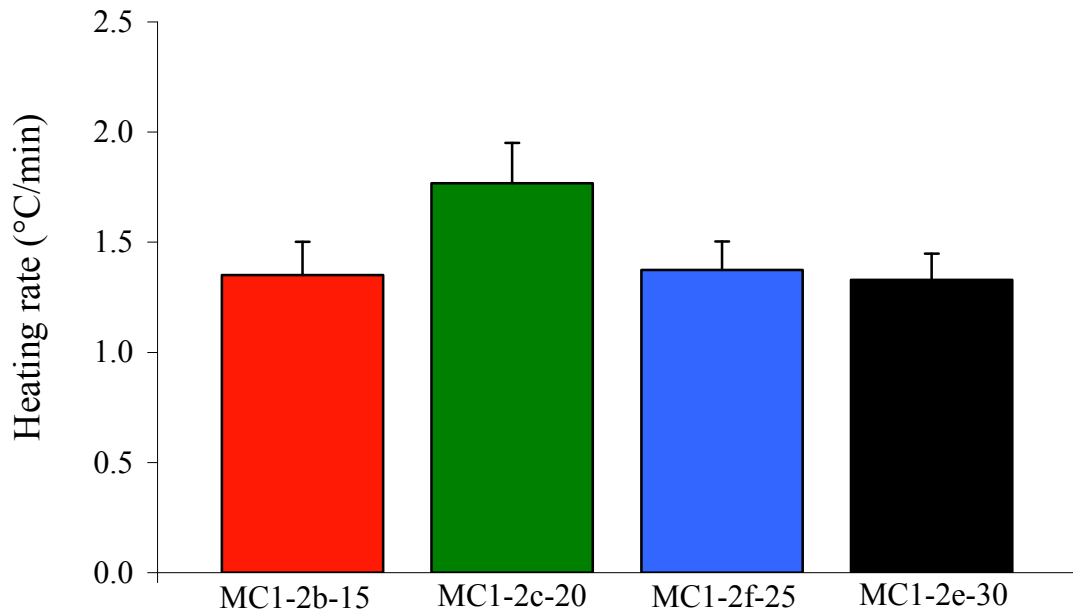


Figure 4-5. Mean heating rates for oil-based ferrofluids. Concentration of ferrofluids was 50 mg/mL canola oil.

Figure 4-6 shows how the iron oxide settled after approximately one week. The effect of settling on the rate of heating can be seen in Figure 4-7.



Figure 4-6. Iron oxide in canola oil after settling for approximately seven days.

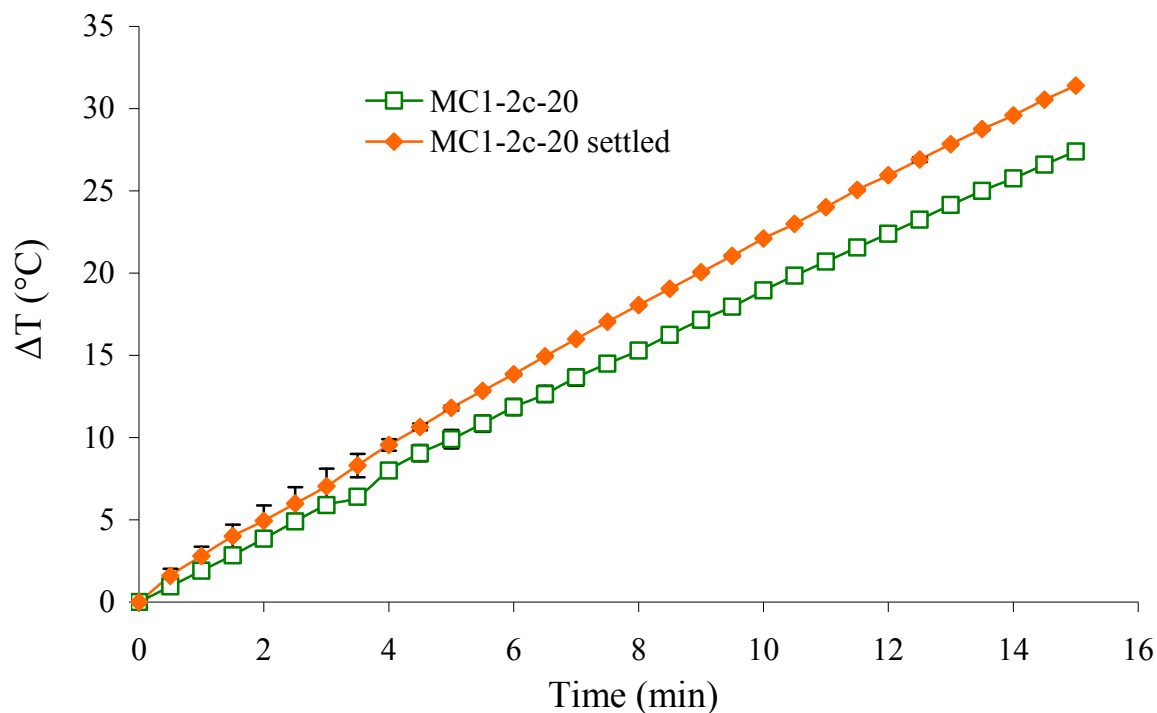


Figure 4-7. Effect of particle settling on heating rate in sample MC1-2c-20.

Discussion

Taking the heating of the control into account, it appears that in heating from room temperature, only MC1-2c-20 would heat to a sufficient degree to induce apoptosis. It appears as if the heating is somewhat independent of starting conditions, however, so it may be possible that in starting from body temperature—approximately 10 to 15°C higher than was seen here—therapeutic temperatures may be possible with the other samples.

Considering the TEM data from chapter 3, it is unclear whether the size of MC1-2c-20 should differ at all from these other samples. As such, without further study it is impossible to say definitively what caused this sample to heat significantly faster than the others tested in this study. If altering the reaction time proves to have little effect when oleic acid is present throughout the reaction, altering the reaction temperature or stirring rate are two potential methods of controlling the balance of nucleation and growth.

While the settling seen in Figures 4-6 and 4-7 can mean some differences in concentration of oxide, it does not mean that there is significant agglomeration. If this were true, the hydrodynamic volume of the particles would increase significantly, resulting in a large decrease in the energy given off while being tested. As shown in Figure 4-7, the opposite is true. The increase seen in practice is in all likelihood due simply to the increase in particle concentration where the thermocouple happened to be situated. As such, it can be concluded that while there is settling to some degree the particles are not agglomerating to any significant degree.

CHAPTER 5 CONCLUSIONS AND FUTURE WORK

Conclusions

The primary problems associated with previous attempts at using SPM ferrofluids with hyperthermia have varied from a poor choice of particle size, inadequate characterization, and/or conditions that would be unsafe for medical use. The various studies reported here attempted to provide a more detailed understanding of each of the factors effecting the heating of SPM ferrofluids. Although not all of the characterization was conclusive, the XANES data showed that there may well be other, less desirable phases present such as goethite. An adjustment of the acidity of the iron chloride solution may be enough to reduce the quantity of goethite, thereby increasing the amount of strongly magnetic material.

Several attempts to adjust the size of the particles were made, adjusting both the reaction time and concentrations of iron chloride. If the TEM micrographs are representative of the samples as a whole, there appears to be a leveling off in particle size. As discussed above, this may be an artifact of settling before the samples were diluted. Further examination with tests such as light scattering, which measure a greater portion of the sample, may be appropriate to determine what is truly occurring. Both changes in concentration and reaction time have been reported in the literature in the past as influencing the size of the particles. Considering this, it is also possible that other factor that is limiting the growth of the particles. The biggest difference with this system in comparison to several in the literature is the presence of oleic acid, which may play a role in favoring nucleation over growth. Controlling this balance appears to be a key factor in controlling particle size. Future adjustments to the temperature of the reaction and stirring rate could possibly alter this balance somewhat.

Despite a significant amount of heating due to the coil itself, at least one of the samples heated to a degree sufficient for use as a hyperthermia treatment. This heating appeared to be repeatable, and not due to settling of particles causing an increase in particle concentration. In addition, the increase in heating when settling did occur lends credence to the idea that while the particles did settle somewhat, they were not agglomerating.

Future Work

The oleic acid, or some kind of surfactant is necessary to prevent agglomeration of the particles. As such, to further study the effect of particle size on heating, other variables such as the temperature of the solution and stirring rate could potentially be examined. Other characterization methods such as light scattering would also be useful in providing a second look at each particle size.

The resonant frequency used in this study is not completely ideal for use with hyperthermia. The resonant frequency is roughly three times what has been established as being the ideal for this purpose. Staying within safe limits, adjusting the frequency in this manner would allow an increase in the magnetic field strength proportional to the decrease in resonant frequency, theoretically increasing the energy given off by the particles by a factor of three. Also, as seen in Figure 4-3, there was a significant amount of heating seen in the control fluid, which contained no magnetic material. Clearly there is too much heat given off by the coil itself. These two factors indicate that if this project is to proceed, a redesign of the coil itself would be beneficial. This redesign should include a change in the physical size of the coil to allow use with animal models and some method of cooling the coil itself.

If any animal studies were to proceed, it would be worth examining the clearance of these smaller particles through the liver. While the literature suggests that particles this small can be digested by the kidney, they must first pass through the healthy liver in order for the treatment to

be useful as designed. If they did not, the delivery mechanism for the particles would have to be redesigned.

LIST OF REFERENCES

1. Pappas SG, Jeruss JS, Talamonti MS. Clinical features of primary and metastatic hepatic malignancies. In: Talamonti MS, Pappas SG, eds. *Liver-directed therapy for primary and metastatic liver tumors*. Kluwer Academic Publishers Group: Norwell, Massachusetts 2001:1-14.
2. Romeo R, Colombo M. The natural history of hepatocellular carcinoma. *Toxicology* 2002;**181-182**:39-42.
3. Ruers T, Bleichrodt RP. Treatment of liver metastases, an update on the possibilities and results. *Eur J Cancer* 2002;**38**:1023-1033.
4. Hugh TJ, Kinsella AR, Poston GJ. Management strategies for colorectal liver metastases-part i. *Surg Oncol* 1997;**6**:19-30.
5. McCarter MD, Fong Y. Metastatic liver tumors. *Semin Surg Oncol* 2000;**19**:177-188.
6. Nordlinger B, Rougier P. Nonsurgical methods for liver metastases including cryotherapy, radiofrequency ablation, and infusional treatment: What's new in 2001? *Curr Opin Oncol* 2002;**14**:420-423.
7. El-Serag HB. Hepatocellular carcinoma and hepatitis c in the united states. *Hepatology* 2002;**36**:S74-S83.
8. El-Serag HB, Mason AC. Rising incidence of hepatocellular carcinoma in the united states. *N Engl J Med* 1999;**340**:745-750.
9. Deuffic S, Buffat L, Poynard T, Valleron AJ. Modeling the hepatitis c virus epidemic in france. *Hepatology* 1999;**29**:1596-1601.
10. Jones SM, Roh MS. Results of surgical resection for hepatocellular carcinoma. In: Talamonti MS, Pappas SG, eds. *Liver-directed therapy for primary and metastatic liver tumors*. Kluwer Academic Publishers Group: Norwell, Massachusetts 2001:59-75.
11. Martinez L, Puig I, Valls C. Colorectal liver metastases: Radiological diagnosis and staging. *Ejso* 2007;**33**:S5-S16.
12. Breasted J. The edwin smith surgical papyrus, vol. 1. University of Chicago: Chicago 1930.
13. Keynes G. The apology and treatise of ambrose pare. Falcon Educational Books: London 1951.
14. Dewhirst MW, Ozimek EJ, Gross J, Cetas TC. Will hyperthermia conquer the elusive hypoxic cell - implications of heat-effects on tumor and normal-tissue micro-circulation. *Radiology* 1980;**137**:811-817.

15. Christophi C, Winkworth A, Muralihdaran V, Evans P. The treatment of malignancy by hyperthermia. *Surgical Oncology-Oxford* 1998;**7**:83-90.
16. Cavaliere R, Ciocatto E, Giovanella B, Heidelberger C, Johnson R, Margottini M, *et al.* Selective heat sensitivity of cancer cells. Biochemical and clinical studies. *Cancer* 1967;**20**:1351-1381.
17. Goldstein LS, Dewhirst MW, Repacholi M, Kheifets L. Summary, conclusions and recommendations: Adverse temperature levels in the human body. *International Journal of Hyperthermia* 2003;**19**:373-384.
18. Sapareto SA, Hopwood LE, Dewey WC, Raju MR, Gray JW. Effects of hyperthermia on survival and progression of chinese-hamster ovary cells. *Cancer Research* 1978;**38**:393-400.
19. Santos-Marques J, Carvalho F, Sousa C, Remiao F, Vitorino R, Amado F, *et al.* Cytotoxicity and cell signalling induced by continuous mild hyperthermia in freshly isolated mouse hepatocytes. *Toxicology* 2006;**224**:210-218.
20. Kampinga HH. Cell biological effects of hyperthermia alone or combined with radiation or drugs: A short introduction to newcomers in the field. *International Journal of Hyperthermia* 2006;**22**:191-196.
21. Hildebrandt B, Wust P, Ahlers O, Dieing A, Sreenivasa G, Kerner T, *et al.* The cellular and molecular basis of hyperthermia. *Critical Reviews in Oncology Hematology* 2002;**43**:33-56.
22. Dewey WC. The search for critical cellular targets damaged by heat. *Radiat Res* 1989;**120**:191-204.
23. Burd R, Dziedzic TS, Xu Y, Caligiuri MA, Subjeck JR, Repasky EA. Tumor cell apoptosis, lymphocyte recruitment and tumor vascular changes are induced by low temperature, long duration (fever-like) whole body hyperthermia. *Journal of Cellular Physiology* 1998;**177**:137-147.
24. Azocar J, Yunis EJ, Essex M. Sensitivity of human natural-killer cells to hyperthermia. *Lancet* 1982;**1**:16-17.
25. Atkinson WJ, Brezovich IA, Chakraborty DP. Usable frequencies in hyperthermia with thermal seeds. *Ieee Transactions on Biomedical Engineering* 1984;**31**:70-75.
26. Moroz P, Jones SK, Gray BN. Tumor response to arterial embolization hyperthermia and direct injection hyperthermia in a rabbit liver tumor model. *Journal of Surgical Oncology* 2002;**80**:149-156.
27. Sugarbaker PH, Vermess M, Doppman JL, Miller DL, Simon R. Improved detection of focal lesions with computerized tomographic examination of the liver using ethiodized oil emulsion (eoe-13) liver contrast. *Cancer* 1984;**54**:1489-1495.

28. Reinig JW, Dwyer AJ, Miller DL, White M, Frank JA, Sugarbaker PH, *et al.* Liver metastasis detection: Comparative sensitivities of mr imaging and ct scanning. *Radiology* 1987;**162**:43-47.
29. Nakakuma K, Tashiro S, Hiraoka T, Ogata K, Ootsuka K. Hepatocellular-carcinoma and metastatic cancer detected by iodized oil. *Radiology* 1985;**154**:15-17.
30. Yumoto Y, Jinno K, Tokuyama K, Araki Y, Ishimitsu T, Maeda H, *et al.* Hepatocellular-carcinoma detected by iodized oil. *Radiology* 1985;**154**:19-24.
31. Moroz P, Jones SK, Metcalf C, Gray BN. Hepatic clearance of arterially infused ferromagnetic particles. *International Journal of Hyperthermia* 2003;**19**:23-34.
32. Le B, Shinkai M, Kitade T, Honda H, Yoshida J, Wakabayashi T, *et al.* Preparation of tumor-specific magnetoliposomes and their application for hyperthermia. *Journal of Chemical Engineering of Japan* 2001;**34**:66-72.
33. Ito A, Shinkai M, Honda H, Kobayashi T. Medical application of functionalized magnetic nanoparticles. *Journal of Bioscience and Bioengineering* 2005;**100**:1-11.
34. Suzuki M, Shinkai M, Honda H, Kobayashi T. Anticancer effect and immune induction by hyperthermia of malignant melanoma using magnetite cationic liposomes. *Melanoma Research* 2003;**13**:129-135.
35. Jiles D. Introduction to magnetism and magnetic materials. Chapman and Hall: London 1991.
36. Morrish AH. The physical principles of magnetism. IEEE Press: New York 2001.
37. Winklhofer M, Fabian, K, Heider, F. Magnetic blocking temperatures of magnetite calculated with a three-dimensional micromagnetic model. *J Geophys Res* 1997;**102**:22,695–622,709.
38. Callister WD. Materials science and engineering: An introduction. 4th ed. John Wiley & Sons, Inc.: New York 1997.
39. Horak D, Lednicky F, Petrovsky E, Kapicka A. Magnetic characteristics of ferrimagnetic microspheres prepared by dispersion polymerization. *Macromolecular Materials and Engineering* 2004;**289**:341-348.
40. Hergt R, Andra W, d'Ambly CG, Hilger I, Kaiser WA, Richter U, *et al.* Physical limits of hyperthermia using magnetite fine particles. *IEEE Transactions on Magnetics* 1998;**34**:3745-3754.
41. Rosensweig RE. Heating magnetic fluid with alternating magnetic field. *Journal of Magnetism and Magnetic Materials* 2002;**252**:370-374.

42. Gonzales M, Krishnan KM. Synthesis of magnetoliposomes with monodisperse iron oxide nanocrystal cores for hyperthermia. *Journal of Magnetism and Magnetic Materials* 2005;**293**:265-270.
43. Leamy PJ. Preparation, characterization, and in vitro testing of poly (lactide-co-glycolide) and dextran magnetic microspheres for in vivo applications [PhD dissertation]. Gainesville: University of Florida; 2003.
44. Chen KZ, Bakuzis AF, Luo WL. Improving surfactant grafting in magnetic colloids. *Applied Surface Science* 2006;**252**:6379-6382.
45. Maity D, Agrawal DC. Synthesis of iron oxide nanoparticles under oxidizing environment and their stabilization in aqueous and non-aqueous media. *Journal of Magnetism and Magnetic Materials* 2007;**308**:46-55.
46. Gnanaprakash G, Mahadevan S, Jayakumar T, Kalyanasundaram P, Philip J, Raj B. Effect of initial ph and temperature of iron salt solutions on formation of magnetite nanoparticles. *Materials Chemistry and Physics* 2007;**103**:168-175.
47. Rizzoni G. Principles and applications of electrical engineering. 4th ed. McGraw-Hill: Boston 2003.

BIOGRAPHICAL SKETCH

John Paul Bullivant was born on December 1, 1976 in Warwick, England, to Keith and Jean Bullivant. After growing up in nearby Leamington Spa, he moved with his family to Gainesville, Florida. In 1995, JP started studying at the University of Florida. He graduated in 1999 with a Bachelor of Science degree in materials science and engineering, specializing in polymer science. While taking time to decide the next steps from here, he worked in Dr. Batich's lab, which led directly to enrollment once again at the University of Florida Department of Materials Science and Engineering in 2001, this time focusing on biomaterials. JP married Jo Aine Clarke on February 9, 2008.